TITLE: APOBEC3A drives deaminase mutagenesis in human gastric epithelium

Running title: APOBEC3A is mutagenic in human cell

AUTHORS

Yohan An[1,10], Ji-Hyun Lee[2,10], Joonoh Lim[1,3,10], Jeonghwan Youk[1,11], Seongyeol Park[1,12], Ji-Hyung Park[1,4], Kijong Yi[1,3], Taewoo Kim[1,13], Chang Hyun Nam[1], Won Hee Lee[1,14], Soo A Oh[3], Yoo Jin Bae[5], Thomas M. Klompstra[2], Haeun Lee[1], Jinju Han[1], Junehwak Lee[6], Jung Woo Park[6], Jie-Hyun Kim[5], Hyunki Kim[7], Hugo Snippert[8], Bon-Kyoung Koo[2,9]*, and Young Seok Ju[1,3]*

1 Graduate School of Medical Science and Engineering, Korea Advanced Institute of Science and Technology (KAIST), Daejeon 34141, Republic of Korea

2 Center for Genome Engineering, Institute for Basic Science, 55, Expo-ro, Yuseong-gu, Daejeon, 34126, Republic of Korea

3 Inocras Inc., 6330 Nancy Ridge Drive, San Diego, CA 92121, United States

4 Department of Neurology, Severance Hospital, Yonsei University College of Medicine, Seoul 03722, Republic of Korea

5 Department of Internal Medicine, Division of Gastroenterology, Gangnam Severance Hospital, Yonsei University College of Medicine, 20, Eonju-ro 63-gil, Gangnam-gu, Seoul 06229, Korea

6 Korea Institute of Science and Technology Information, Daejeon 34141, Republic of Korea

7 Department of Pathology, Yonsei University College of Medicine, Seoul 03722, Republic of Korea

8 Oncode Institute, Center for Molecular Medicine, University Medical Center Utrecht, 3521 AL Utrecht, the Netherlands

9 Department of Life Sciences, Pohang University of Science and Technology (POSTECH), Pohang, 37673, Republic of Korea

10 These authors contributed equally

* Correspondence: ysju@kaist.ac.kr(Y.S.J.); koobk@ibs.re.kr(B.-K.K)

Present address

11 Division of Hematology and Medical Oncology, Department of Internal Medicine, Seoul National University College of Medicine and Seoul National University Hospital, Seoul, 03080, Republic of Korea

12 Stanford Cancer Institute, Stanford University School of Medicine, Stanford, CA, 94305, USA

13 Center for Neurogenetics, Brain and Mind Research Institute, Weill Cornell Medicine, New York, NY 10044, USA

14 Department of Radiation Oncology, Yonsei Cancer Center, Heavy Ion Therapy Research Institute, Yonsei University College of Medicine, Seoul 03722, Republic of Korea

Corresponding authors

Bon-Kyoung Koo, PhD.

koobk@ibs.re.kr

Director

Center for Genome Engineering, Institute for Basic Science, 55, Expo-ro, Yuseong-gu, Daejeon, 34126, Republic of Korea

Young Seok Ju, MD, PhD.

ysju@kaist.ac.kr

Professor

Graduate School of Medical Science and Engineering, Korea Advanced Institute of Science and Technology (KAIST), Daejeon 34141, Republic of Korea

ABSTRACT

Cancer genomes frequently carry APOBEC (apolipoprotein B mRNA editing catalytic polypeptide-like)-associated DNA mutations, suggesting APOBEC enzymes as innate mutagens during cancer initiation and evolution. However, the pure mutagenic impacts of the specific enzymes among this family remain unclear in human normal cell lineages. Here, we investigated the comparative mutagenic activities of *APOBEC3A* and *APOBEC3B*, through whole-genome sequencing of human normal gastric organoid lines carrying doxycycline-inducible APOBEC expression cassettes. Our findings demonstrated that transcriptional upregulation of *APOBEC3A* led to the acquisition of a massive number of genomic mutations in just a few cell cycles. By contrast, despite clear deaminase activity and DNA damage, *APOBEC3B* upregulation did not generate a significant increase in mutations in the gastric epithelium. *APOBEC3B*-associated mutagenesis remained minimal even in the context of TP53 inactivation. Further analysis of the mutational landscape following *APOBEC3A* upregulation revealed a detailed spectrum of *APOBEC3A*-associated mutations, including indels, primarily 1bp deletions, clustered mutations, and evidence of selective pressures acting on cells carrying the mutations. Our observations provide a clear foundation for understanding the mutational impact of APOBEC enzymes in human cells.

INTRODUCTION

Large-scale cancer genome studies have revealed various mutational processes in human somatic cells (Alexandrov et al. 2020). APOBEC enzymes, originally known for cytosine deamination in the DNA and RNA against pathogens (Vieira and Soares 2013), were concluded as major endogenous mutagens in cancer (Nik-Zainal et al. 2012b, 2012a; Roberts et al. 2013; Lawrence et al. 2013). About 75% of human cancer types, including bladder transitional cell carcinoma (98%, 381 of 389 samples), breast adenocarcinoma (83%; 759 of 915 samples), and stomach adenocarcinoma (21%; 101 of 486 samples) showed APOBEC-associated mutational patterns (Sondka et al. 2024). In parallel, the APOBEC-associated mutations are also observed in non-neoplastic normal cells, particularly within the epithelium of the bladder, bronchus, and small intestine (Lawson et al. 2020; Wang et al. 2023; Yoshida et al. 2020). Their mutational spectra, predominantly C>T and C>G base substitutions enriched in TpCpN context (with the mutated cytosine is underlined), corresponds to COSMIC signatures SBS2 and SBS13 (https://cancer.sanger.ac.uk/signatures/). Of the 11 APOBEC family genes in the human genome, *APOBEC3A* (**A3A**) and *APOBEC3B* (**A3B**) have been suggested as major potential contributors to the APOBEC-associated mutations in most human cell types (Chan et al. 2015; Roberts et al. 2013) along with *APOBEC1* in the small intestine (Wang et al. 2023).

The mutagenic potential of A3A and A3B has been investigated across a range of human cancer cell lines (Burns et al. 2013; Carpenter et al. 2023; Petljak et al. 2022). In doing so, APOBEC-associated mutagenic activity has been proposed to occur episodically in cancer cell line models (Petljak et al. 2019). In addition, non-human model systems, such as *Mus musculus, Saccharomyces cerevisiae,* and the cell line derived from *Gallus gallus domesticus,* have also been utilized for exploring the mutagenic impact of APOBEC enzymes (Durfee et al. 2023; DeWeerd et al. 2022; Naumann et al. 2023; Law et al. 2020; Chan et al. 2015). However, these systems are suboptimal, as these models carry

confounding factors, such as additional oncogenic alterations or non-human genomic backgrounds. To isolate the pure mutagenic activity of A3A and A3B in human normal cells, we explored genomic alterations in human non-neoplastic gastric organoid lines following APOBEC upregulation, using single-cell cloning and whole-genome sequencing (**WGS**; Jager et al. 2019; Pleguezuelos-Manzano et al. 2020; Youk et al. 2024) as well as duplex DNA sequencing (Hoang et al. 2016).

RESULTS

Gastric organoids with doxycycline-inducible APOBEC genes

We established human gastric organoid lines with doxycycline-inducible expression of either A3A or A3B, referred to as hGO_{iA3A} and hGO_{iA3B}, respectively. In these lines, doxycycline treatment simultaneously induces (1) mCherry fluorescence, and (2) expression of the corresponding APOBEC enzyme. To this end, we integrated two cassettes into the genome of gastric organoids, (1) expressing rtTA and hygromycin B resistance protein (CMV-*rtTA*-*HygR*), and (2) expressing APOBEC enzymes and fluorescence protein (TRE-APOBEC (*A3A* or *A3B*)-IRES-*mCherry*) using the *piggyBac* transposon system (**Fig. 1A**; Woodard and Wilson 2015; Wilson et al. 2007). Successfully engineered organoids were selected using hygromycin treatment and subsequently constructed into clonal lines. WGS confirmed their single-cell origin (**Supplemental Fig. S1**), the copy number and genomic positions (**Supplemental Tables S1, S2**), and the correctness of the reading frame of the APOBEC gene in the integrated cassettes (**Supplemental Fig. S2**).

Upon doxycycline treatment, mCherry fluorescence as well as APOBEC upregulation were clearly detected within 48 hours (**Fig. 1B,C**). Here, we treated 0.1 µg/ml and 3 µg/ml of doxycycline for low- and high-level induction, respectively. Gene expression levels of induced A3A or A3B ranged from 400 to 6,000 transcripts per millions (**TPMs**), representing

a several hundred-fold increase over endogenous levels (**Fig. 1D; Supplemental Fig. S3**). Of note, endogenous APOBEC transcripts minimally contributed less than 0.2% of the total APOBEC transcripts (**Supplemental Table S3**).

Single-cell transcriptome data from various cancer types indicated that the range of APOBEC expression levels observed in our models were comparable to those observed during episodic bursts in many cancer types, including lung adenocarcinoma, head-and-neck squamous cell carcinoma, triple-negative breast cancer, esophageal adenocarcinomas and squamous cell carcinomas (**Supplemental Fig. S4;** Karaayvaz et al. 2018; Maynard et al. 2020; Puram et al. 2017; Wu et al. 2018). Unfortunately, expression levels in gastric adenocarcinoma could not be explored due to the lack of available single-cell Smart-seq data.

Following A3A or A3B induction, the viability of the organoid lines was substantially compromised, suggesting a detrimental impact of APOBEC upregulation on cell survival (**Fig. 1E**). After APOBEC induction, differentially expressed genes included those involved in the cell cycle (e.g., *CDKN1A* and *CDC20*) and immune response (e.g., *CXCL8* and *CCL20*) in both the hGO_{iA3A} and hGO_{iA3B} models (**Fig. 1F;** Cazzalini et al. 2010; Amador et al. 2007; Matsushima et al. 2022; Wu et al. 2007). The induced APOBEC enzymes predominantly localized to the nuclei and led to an increase in γ-H2AX foci, suggesting APOBEC-induced DNA damage, such as replication stalling or double-strand breaks (**DSBs**), as previously reported (**Fig. 1G,H**; **Supplemental Fig. S5**; Burns et al. 2013; Green et al. 2016).

APOBEC3A, not APOBEC3B, induces genomic mutations

To assess the mutagenic impacts of A3A and A3B, we investigated acquired mutations in the hGO_{iA3A} and hGO_{iA3B} lines after 48 hours of doxycycline treatment. On average, the hGO_{iA3A} lines treated with 0.1 µg/ml and 3 µg/ml doxycycline exhibited 267 and 2,448 SBS2/13 base substitutions genome-wide, respectively (0.1 µg/ml: 95% CI, 107-505; 3 µg/ml: 95% CI, 1,052-3,708; **Fig. 2A,B,F**; **Supplemental Tables S4, S5**). By contrast, the hGO_{iA3B}

clones showed a negligible number of APOBEC-associated mutations following induction (0.1 µg/ml: 95% CI, 0-1; **Fig. 2A,D,F**; **Supplemental Tables S4, S5**).

To minimize potential detection bias in our single-cell cloning system, where proliferative cells are preferentially sequenced, we employed duplex DNA sequencing (Hoang et al. 2016), which precisely captures non-clonal mutations across the entire cell population, including those confined to single cells that could not proliferate further. The mutational burden per diploid genomes from the duplex DNA sequencing revealed a time-dependent increase in A3A-associated mutations following doxycycline treatment, ultimately resulting in higher levels than those observed from the clones (0.1 µg/ml: 95% CI, 4,590-6,038; 3 µg/ml: 95% CI, 9,316-10,077; **Fig. 2A,C**; **Supplemental Table S6**). In contrast, but in line with our observation from the clones, APOBEC-associated base substitutions in hGO_{iA3B} lines remained minimal in duplex sequencing (0.1 µg/ml: 95% CI, 136-352; 3 µg/ml: 95% CI, 79-133; **Fig. 2A**; **Supplemental Table S6**). Of note, unlike hGO_{iA3A}, we did not detect A3B-associated mutations even at earlier time points (**Fig. 2E**), suggesting that the absence of mutations in hGO_{iA3B} is unlikely to be due to the negative selection against hypermutated cells. Our findings overall indicate that A3B alone does not act as a major mutator, at least in human normal gastric epithelium.

Despite the absence of fixed mutations in hGO_{iA3B} models, the A3B enzyme in cell lysates was fully functional, exhibiting strong cytosine deamination activity for extracellular DNA oligonucleotides *in vitro* (**Fig. 3A**). Denatured genomic DNA fragments exposed to recombinant A3B enzymes underwent near-complete deamination of unmethylated (non-CpG) cytosines (~99%) upon contact with the enzyme (**Fig. 3B,C**). This activity was further confirmed in the duplex DNA sequencing, where lysates from hGO_{iA3B} induced a substantial number of C>T artifacts during library preparation, particularly in the 5' head region (~50 bp) of the sequencing reads with a clear positive correlation with the doxycycline concentration, as reported previously (**Supplemental Fig. S6A,B**; Abascal et al. 2021). Finally, the increase in γ-H2AX foci in the hGO_{iA3B} following doxycycline induction (**Fig. 1H;**

Supplemental Figure S5) also indicates DNA damage consistent with A3B activity. Collectively, our findings strongly indicate that gastric organoids either efficiently repair A3B-induced lesions or possess intrinsic mechanisms that suppress A3B-associated cytosine deamination in the nucleus.

To further investigate whether inactivation of tumor suppressor genes accelerates APOBEC-associated mutagenesis, we generated the hGO_{iA3A} and hGO_{iA3B} lines carrying biallelic truncating mutations in *TP53* (hereafter referred to as TP53KO-hGO_{iA3A} and TP53KO-hGO_{iA3B}, respectively; **Fig. 1A**). In the TP53KO-hGO_{iA3A} lines, we observed a similar burden of APOBEC-associated mutations as that observed in the hGO_{iA3A} lines (0.1 µg/ml: 95% CI, 785-1,917; 3 µg/ml: 95% CI, 152-3,091; **Fig. 2A,B**; **Supplemental Table S5**). The TP53KO-hGO_{iA3B} lines exhibited a lack of APOBEC-associated mutations consistent with the hGO_{iA3B} lines (0.1 µg/ml: 95% CI, 11-19; 3 µg/ml: 95% CI, 2-12; **Fig. 2A,D**; **Supplemental Table S5**). Taken together, these findings imply that the inactivation of TP53 does not promote APOBEC-associated mutagenesis in gastric organoids.

Despite the increased γ-H2AX foci following A3A or A3B overexpression (**Fig. 1H**; **Supplemental Fig. S5**), which often indicate DNA DSBs, we did not observe a remarkable increase of structural variations (**SVs**; **Supplemental Table S5**) in all the clones including TP53KO-hGO_{iA3A} and TP53KO-hGO_{iA3B} lines. These findings indicate that APOBEC-induced DSBs or replication stalls are efficiently repaired within gastric organoids.

Both APOBEC3A and APOBEC3B induce C>U RNA editing

Despite their contrasting mutagenic impact on DNA, both enzymes exhibited C>U RNA editing events. In RNA sequencing normalized to a total base count of 3.1Gb, both the hGO_{iA3A} and hGO_{iA3B} lines showed an approximately 8-fold and 30-fold increases in C>U RNA editing sites, following 0.1 µg/ml and 3 µg/ml doxycycline treatment for 48 hours, respectively (**Fig. 2G,I**; **Supplementary Fig. S7A; Supplemental Table S7**).

The spectra of C>U RNA-editing deviated from SBS2 associated with DNA mutations, and also varied between A3A and A3B (**Fig. 2H,J**). Briefly, (1) both A3A and A3B exhibited reduced specificity for the UpCpU context (TpCpT in DNA). However, (2) A3A displayed enhanced specificity for the UpCpG context (TpCpG in DNA), and (3) A3B showed increased specificity for contexts other than UpCpN (non-TpCpN in DNA).

Further *de novo* decomposition of RNA editing spectra revealed three RNA editing signatures, referred to as RNA-SBS_A, RNA-SBS_B, and RNA-SBS_C, corresponding to A3A-, A3B- and ADAR (Adenosine Deaminase Acting on RNA)-associated A-to-I RNA editing, respectively (**Supplemental Fig. S8A,B**). Though RNA-SBS_A was overall consistent with an A3A-associated RNA-editing spectrum previously reported (Martínez-Ruiz et al. 2023; Fixman et al. 2024), RNA-SBS_B was slightly different from one for A3B established from *Mus musculus* (Alonso de la Vega et al. 2023). Spectra in pentanucleotide contexts further showed that A3A-associated RNA editing was preferentially enriched in ApUpCpApN (ApTpCpApN in DNA) and ApUpCpGpN (ApTpCpGpN in DNA) contexts, whereas A3B-associated editing did not show such an enrichment (**Supplemental Fig. S9**).

The C>U RNA editing sites were frequently recurrent, particularly among the sites identified in the low doxycycline concentration (**Supplemental Fig. S7B**). Of the 16,574 C>U RNA editing sites detected across all samples, 7,593 (45.8%) were recurrent, or observed in more than one sample (**Supplemental Fig. S7C-E; Supplementary Table S8**), suggesting that these were C>U RNA-editing hotspots. Of these, 3,769 and 2,769 were exclusively identified in hGO_{iA3A} and hGO_{iA3B} lines, respectively (**Supplemental Fig. S7D,F**).

A3A-associated RNA editing hotspots were enriched in specific sites in the secondary stem-loop structure of RNAs, including the 3rd, 4th and 4th positions of the 3bp, 4bp, and 5bp RNA-loop structures, respectively, as reported previously (**Supplementary Fig. S7G**; Jalili et al. 2020). Further, we found an enrichment in specific positions of the larger loops (**Supplementary Fig. S7G**). In contrast, A3B-associated RNA editing hotspots did not show

site preferences in the RNA-loop structures (**Supplementary Fig. S7G**). The lower context stringency in A3B may be caused by the structural differences of α1/loop-1 and β-2 residues of the CD2 domain (Kim et al. 2023).

Characteristics of APOBEC-associated mutations

Using the pure A3A-mediated mutational profiles from hGO_{iA3A} lines, we examined the detailed characteristics of A3A-associated mutational signatures. These analyses could not be applied to A3B due to the near absence of A3B-associated mutations in this study (**Supplemental Fig. S10A-C**). A3A-associated mutations in the TpCpA context were 2.7 times more abundant following pyrimidine bases (YpTpCpA) compared to purine bases (RpTpCpA; **Fig. 4A**). Of note, the RpTpCpA sequence context has been reported as a preferred motif for A3B-associated mutations in the *Saccharomyces cerevisiae* and *in vitro* model (Chan et al. 2015; Sanchez et al. 2024). The YpTpCpA preference in our study closely mirrors the enrichment level observed in human cancer tissues carrying APOBEC-induced hypermutations (YpTpCpA/RpTpCpA = 2.5 in cancers with SBS2/13 burdens > 5,000 genome-wide), indicating that A3A could be a key enzyme of the APOBEC-associated hypermutations in most human cancers.

Further, in line with previous reports from cancer (DeWeerd et al. 2022), indels attributable to the COSMIC ID9 signature (Sondka et al. 2024) showed a suggestive positive correlation with the number of A3A-associated base substitutions in hGO_{iA3A} clones, one per 333 SBS2/13 base substitutions (**Fig. 4B**; p-value = 0.051). Of note, base substitutions attributable to clock-like mutational signatures (SBS5 and SBS40) demonstrated a positive correlation with the burden of A3A-associated base substitutions (SBS2 and SBS13; **Fig. 4C**), suggesting that A3A-induced genomic damage indirectly promotes error-prone DNA repair processes across the genome. However, this association was absent in hGO_{iA3A} clones carrying *TP53* truncating mutations (**Fig. 4C**). We speculate that this difference reflects differential DNA repair pathways according to the activities of TP53 (Kim et al. 2016).

Notably, among the polymerases encoded in the human genome, increased transcription of DNA polymerase eta (*POLH*), which is involved in translesion synthesis (**TLS**; Choi and Pfeifer 2005; Delbos et al. 2005), was exclusively observed in clones with functional TP53 (**Fig. 4D; Supplemental Fig. S11**). Previously, *REV1*, a component of the TLS pathway, was shown to contribute to the generation of SBS5 and SBS40 in cancer cell lines (Petljak et al. 2022). Collectively, this suggests that the TLS machinery may contribute to the mutational processes underlying SBS5 and SBS40.

Clusters of APOBEC-associated mutations

In cancer genomes, APOBEC-induced localized hypermutation events are frequently observed (Nik-Zainal et al. 2012a; The ICGC/TCGA Pan-Cancer Analysis of Whole Genomes Consortium 2020). Across the mutations detected in our hGO_{iA3A} and TP53KO-hGO_{iA3A} lines, approximately 5% of the 29,650 acquired base substitutions were clustered within 1 kbp, which is ~100-fold higher than expected by chance (**Fig. 5A**). Such clustered mutation events can be classified as either *omikli* and *kataegis*, based on the density (Bergstrom et al. 2022b). Overall, we detected 615 *omikli* and 109 *kataegis* events. The observed *kataegis* events ranged from 4 to 22 base substitutions (median = 5). The absence of correlation between the clustered mutations in this study and complex genomic events indicate that those were driven by the pure activity of A3A. For instance, SV-associated *kataegis*, which consists of ~36% of *kataegis* events in cancer genomes (The ICGC/TCGA Pan-Cancer Analysis of Whole Genomes Consortium 2020; Bergstrom et al. 2022b; Nik-Zainal et al. 2012a), were rare in our data (2.8%; 3 out of 109 events). Similarly, the *kataegis* in our clones were independent of other known *kataegis*-inducing genomic events, such as anaplastic DNA bridges (Maciejowski et al. 2020) and extrachromosomal DNA (ecDNA; Bergstrom et al. 2022b).

The relative frequencies of *omikli* and *kataegis* remained consistent at 2.4% (95% CI: 1.7-3.1%) and 0.4% (95% CI: 0.22-0.58%) of all A3A-associated mutation events, respectively,

with each isolated and clustered mutation counted as a single event (**Fig. 5B**; **Supplemental Table S9**). These ratios were more or less constant among clones, regardless of the doxycycline concentration, or *TP53* mutational status. Notably, the frequencies of *omikli* and *kataegis* were comparable to the SV-unrelated *omikli* and *kataegis* frequencies in cancers (**Fig. 5B**; **Supplemental Table S9**).

Within *kataegis* regions, cytosine alterations did not always occur in the TpCpN context. We observed that ~7% of cytosine substitutions occurred in non-TpCpN context (39 out of 556 mutations; **Fig. 5C**), about twofold higher than expected on SBS2 and SBS13 signatures (7.00% vs. 3.33%; chi-square test, $p<0.005$). Our data indicated that these non-TpCpN mutations are not independent to, but are part of *kataegis* for two reasons: (1) non-TpCpN mutations were 267-fold more abundant than observed in the background regions (**Fig. 5D**); and (2) non-TpCpN mutations within *kataegis* regions were completely phased with other classical TpCpN mutations on the same allele (27 out of 27), where only 50% phasing would be expected by chance. This suggests that DNA repair mechanisms for cytosine deamination in non-TpCpN contexts are less accurate in the mutagenesis of clustered mutations.

Of the 615 *omikli* and 106 *kataegis* events (excluding three *kataegis* events associated with rearrangements*)*, approximately 5% (35 *omikli* and 5 *kataegis* events) exhibited strand-switching of the mutated cytosines between parental and daughter strands during replication (**Fig. 5E,F**). In one *kataegis* event, composed of 9 base substitutions (in clone A3A_1st_C3_3µg-5), we observed five strand-switching events (**Fig. 5G**). Phasing analysis revealed that clustered mutations on both DNA strands occurred on the same allele (26 out of all 26 informative events). Additionally, the mutational spectrum of the minorly contributing strand was predominantly composed of mainly C>T or C>G mutations in the TpCpN context (62%; 13 out of 21 mutations; **Fig. 5C**), implying that all the mutations were APOBEC-associated. Besides, the rate of TpCpN mutations in the minor strand within strand-switching *kataegis* regions was 124-fold higher than randomly expected (**Fig. 5H**). Although the

underlying mechanism remains unclear, our findings indicate that strand-switching of the A3A enzyme should be possible when generating clustered mutations during replication (**Fig. 5F**).

Epigenetic contexts associated with A3A-associated mutations

Mutational processes are often influenced by the epigenetic contexts of the genome (Otlu et al. 2023). Of the 14 genomic features examined, three features (replication timing, local transcription level, and H3K27me3) showed potential associations with local A3A-associated mutational burdens (**Fig. 6A**). Of the three features, replication timing and local gene transcription level demonstrated consistent trends correlating with A3A-associated mutation rates (**Supplemental Table S10**).

For the replication timing, the latest-replicating regions showed a 1.26-fold higher rate of A3A-associated mutation compared to the earliest-replicating regions (**Fig. 6B**) as previously reported (Kazanov et al. 2015). This may be attributed to the DNA repair mechanisms, including base excision repair, which are particularly active in early-replicating regions consisting of open chromatin (Amouroux et al. 2010; Rhind and Gilbert 2013). Further, the A3A-associated mutation rate in the lagging strand of DNA replication was 1.26-fold higher compared to the leading strand (**Fig. 6C**), which presumably originated from more frequent exposure of single-stranded DNA (ssDNA) induced by Okazaki fragments in the lagging strand (Wu et al. 2020), similar with previous elucidation (Hoopes et al. 2016). In addition, mutation rates in genic regions were correlated with expression levels (**Fig. 6D**), showing a 1.37-fold higher mutation rate in actively transcribed genomic regions compared to silent genic regions, consistent with the previous studies (Kazanov et al. 2015; Nordentoft et al. 2014). Of note, the lagging strand and highly transcribed genes tend to be more frequently single-stranded than the leading strand and silent genes (Okazaki et al. 1968; Gnatt et al. 2001), which may make them more susceptible to A3A-induced DNA damage, respectively. The results demonstrated that DNA regions with frequent ssDNA exposure have a higher

chance of being damaged by A3A. In line with this observation, the non-transcribed genic strand was mutated 1.13-fold more frequently than the transcribed strand (**Fig. 6E**), consistent with a previous report (Saini et al. 2017).

Compared with non-coding sequences, protein-coding sequences showed much lower mutation rates, at 0.79-fold the genome average, suggesting a selective pressure against mutations that could alter amino-acid-changing mutations (**Fig. 6F**). Of note, in TP53-inactivated clones (TP53KO-hGO$_{iA3A}$ clones), mutation rates in protein-coding regions slightly increased to 0.834-fold of the genome average, potentially due to reduced negative selection pressures in the absence of functional *TP53*.

DISCUSSION

Our study clearly demonstrated the qualitative and quantitative mutational impact of A3A and A3B in human non-neoplastic cells using a gastric organoid culture system. Previous studies have highlighted the mutagenic potential of A3B in various model systems (Dananberg et al. 2024; Carpenter et al. 2023; Durfee et al. 2023; Chan et al. 2015). In contrast, a recent study suggested only a modest contribution of A3B mutagenesis in human cancer cell lines (Petljak et al. 2022). To our knowledge, our study is the first to directly assess the mutagenic activity of A3B in human normal cells.

The gastric organoid model offered distinct advantages based on three key criteria : (1) biological relevance, supported by the frequent occurrence of APOBEC-associated mutations in gastric cancers, (2) experimental feasibility, owing to its robust proliferative capacity under culture conditions, and (3) the availability of standardized protocols for genetic manipulation (Fujii et al. 2015; Gaebler et al. 2020). For example, despite the high prevalence of APOBEC-associated mutations in breast and lung cancers, the corresponding normal epithelial cells are suboptimal for this study due to their limited proliferative capacity in organoid culture as well as their poor compatibility with genetic engineering.

When A3A was induced by 3 µg/ml of doxycycline in hGO_{iA3A} lines, transcription was activated for ~2-3 days, reaching peak expression levels of ~800 TPM. Under these conditions, we detected ~2,500 A3A-induced base substitutions in proliferative clones, suggesting that ~1,000 base substitutions could be acquired in a day. These findings support the notion that a transcriptional burst of A3A can also lead to a massive number of mutations in normal gastric epithelium as well, consistent with previous observations in cancer (Petljak et al. 2019). However, the frequency of episodic A3A upregulation *per se* is unknown in human normal gastric epithelium. According to conventional wisdom, APOBEC overexpression is thought to be associated with viral infection. However, publicly available transcriptomic data from SARS-CoV-2-infected human gastric organoids revealed no substantial upregulation of A3A or A3B (**Supplemental Fig. S12**; Giobbe et al. 2021).

Our models also indicated increased mutational burdens of SBS5 and SBS40 proportional to the overall burden of A3A-associated mutations, suggesting base substitutions attributable to other than SBS2 and SBS13 can also be indirectly promoted in APOBEC upregulation. These signatures were significantly enriched in late-replicating regions and correlated with multiple epigenomic features, including replication timing and transcriptional activity, in line with previous reports (**Supplemental Fig. S13A,B;** Sondka et al. 2024).

Although this study successfully evaluated the mutagenic activity of A3A and A3B in human normal cells, several technical limitations warrant consideration. First, the study was primarily conducted using gastric epithelial cells, and we cannot exclude the possibility that A3B may exhibit substantial mutagenic activity in other cell types. Second, the endogenous copies of A3A and A3B were not inactivated in the hGO_{iA3A} and hGO_{iA3B} models, raising the possibility that a minor fraction of the observed APOBEC-associated mutations and RNA editing sites may have originated from native enzymes. Third, the inclusion of additional control models, such as catalytically inactive mutants (for example, A3A-E72A and A3B-E255A; Carpenter et al. 2023) or APOBEC-enzyme inhibitors, would further clarify the mechanisms underlying APOBEC overexpression. Finally, our genomic analyses were

384 conducted using an earlier version of the human reference genome (GRCh37), due to the
385 dependency of our somatic mutation calling pipeline using previously constructed large-
386 scaled unmatched normal sample matrix based on the GRCh37 sequences (Park et al.
387 2021). Nonetheless, our findings remain consistent in the benchmark analysis with the latest
388 reference (GRCh38; **Supplemental Fig. S14**).

METHODS

Materials Availability

Organoids established in this study will be available under a material transfer agreement. To do so, please contact the lead author (ysju@kaist.ac.kr).

Human normal gastric samples

Normal gastric tissues were obtained via endoscopic biopsy from a female undergoing routine screening. The protocol for this study was approved by the Institutional Review Board of Yonsei University Gangnam Severance Hospital (3-2018-0207) and KAIST (KH2022-211).

Human stomach organoid culture

Organoid culture methods and media compositions were adopted from previous research with slight modifications (Bartfeld et al. 2015). Wnt3A- and R-spondin 1-conditioned media were produced with HEK293 cell line producing Afamin-Wnt3a (Mihara et al. 2016) and Cultrex HA-R-Spondin 1-Fc 293T cell line (Trevigen, 3710-001-01).

Tissues were incubated in TrypLE (Gibco, Cat No.12604013) at 37°C for 30 minutes, then dissociated into clusters of 10-15 cells by pipetting. After watching with PBS twice and centrifugation at 300g for 5 minutes at 4°C, pellets were resuspended in cold Matrigel (Corning, Cat No.BDL356231) and seeded in 12- or 24-well plates (Merck). Following a 10-mute incubation at 37°C in 5% CO_2, 0.5-1 ml of prewarmed culture medium was added. Medium was changed every 2-3 days. Organoids were passaged every two weeks using Cell Recovery solution (Corning, Cat No.354253) and Accutase (Stemcell Technology, Cat No.07922; see **Supplemental Methods; Supplemental Table S11**).

Preparation of vectors for transfection

Two vectors were purchased: (1) CMV-*rtTA-HygR* vector (Addgene, Cat No.102423) and (2) CRISPR-*Cas9* vectors containing gRNA sequence for *TP53* (Addgene, Cat No.121917). To generate the pPB-CMVmin-APOBEC (*A3A* or *A3B)*-IRES-*mCherry* vectors, APOBEC constructs were designed with the *APOBEC3A* (NM_145699.4) and *APOBEC3B* (NM_004900.4) sequences and cloned into the vector backbone containing Tet-on system cassette (pPB-CMVmin-TRE-IRES-*mCherry;* see **Supplemental Methods;** Lee et al. 2022).

Transfection of organoids

Transfection methods were adopted from previously reported protocols (Gaebler et al. 2020; Fujii et al. 2015). A mixture of three kinds of vectors was utilized: (1) TRE-APOBEC (*A3A* or *A3B*)-IRES-*mCherry* cassette, (2) CMV-*rtTA-HygR*, and (3) piggyBac transposase cassette. Resuspended organoids in Opti-MEM (Gibco, Cat No.31985062) or BTXpress buffer (BTX) were mixed with a vector cocktail. Electroporation was performed using a previously described program from the literature (see **Supplemental Methods**; **Supplemental Table S12;** Fujii et al. 2015). Selection was carried out for one week with 1 µg/ml hygromycin (InvivoGen, Cat No.ant-hg-1). Single-cell cloning was performed using FACSAriaII (BD Biosciences), followed by manual picking of organoids derived from single cells by pipetting (Youk et al. 2021).

Doxycycline treatment

A doxycycline (Sigma-Aldrich., Cat No.D9891-1G) stock solution was prepared by dissolving doxycycline in the DMSO. Prior to treatment, dissociated 10k viable cells were seeded in 24-well the plates. After 7 days, doxycycline solution was added to the medium, and the organoids were incubated with doxycycline.

Capturing fluorescent images

mCherry fluorescence following doxycycline treatment was visualized using a fluorescence microscope (LEICA, DMi8). Fluorescent images were captured using Las X programs, and brightness/contrast adjustments were applied using the same program.

Preparation of cell lysates

Organoids treated with 3 µg/ml doxycycline were harvested using Cell Recovery solution (Corning), followed by one wash with PBS. The isolated cell pellets by centrifugation were resuspended in lysis buffer containing 25 mM HEPES (pH 7.9), 10% glycerol, 150 mM NaCl, 0.5% Triton X-100, 1 mM EDTA, 1mM MgCl2, 1 mM ZnCl2, RNase A (0.2 mg/ml; Thermo Scientific, EN0531), and 1× protease inhibitors (Thermo Scientific, 877885). Cell lysates were then sonicated, incubated on ice for 30 minutes, and centrifuged at 13,000 rpm at 4°C for 10 minutes. The supernatant was collected, and protein concentration was measured with Qubit™ Protein and Protein Broad Range (BR) Assay Kits (Thermo Scientific, Q33211).

Western blotting

Lysates were prepared with mixing samples 1:1 with Laemmli Sample Buffer (Bio-Rad, #161-0737), followed by denaturation at 95°C for 5 minutes. Proteins were separated by SDS-PAGE on a Mini-PROTEAN® TGX™ pre-cast 12% gel (Bio-Rad, 4561044) in SDS running buffer (Higene™, PB151-10h) and transferred to an Immobilon® PVDF membrane (Millipore, IPFL00010) via overnight wet transfer in Tris/Glycine buffer (Bio-Rad, #1610771).

Primary antibodies included Anti-HA.11 Epitope Tag Antibody (1:5000; BioLegend, 951514) and Anti-α-Antin-1 (1:1000, Sigma-Aldrich, A2066). HRP-conjugated secondary antibodies were used at 1:2000 dilution: goat anti-mouse IgG-HRP for Anti HA (Santa Cruz, sc-2005) and goat anti-rabbit IgG-HRP for AntiActin (Santa Cruz, sc-2004) were utilized for secondary antibodies (see **Supplemental Methods**).

Whole transcriptome sequencing library construction

RNA was isolated during DNA extraction for BotSeqS libraries with AllPrep DNA/RNA Mini kit, following the manufacturer's instructions. Libraries were constructed with the NEBNext Ultra II Directional DNA Library Prep Kit for Illumina (NEB, Cat No.E7760) and the QiAseq FastSelect -rRNA HMR kit (Qiagen, Cat No.334388), according to manufacturers' instructions. Libraries were sequenced on the NovaSeq 6000 with paired-end sequencing.

Calculating RNA expression level

Bulk RNA-seq reads were aligned to GRCh37 using STAR2 v2.6.1d (Dobin et al. 2013). TPM and read counts were calculated with RSEM v1.3.1 (Li and Dewey 2011). Differential expression gene analysis was conducted using the DESeq2 package in R (Love et al. 2014).

Calculation of ratio between endogenous APOBEC mRNA and overexpressed APOBEC mRNA

Sequence differences between the endogenous and overexpressed mRNA were utilized for counting (see **Supplemental Methods**). The proportion of endogenous mRNA was estimated by calculating the ratio of supporting reads.

Analysis of A3A and A3B expression levels in single cancer cells with public scRNA data

Publicly available single-cell RNA-seq datasets, generated with Smart-seq library, from lung adenocarcinoma, triple negative breast cancer, esophageal adenocarcinoma and esophageal squamous cell carcinoma were analyzed using the same pipeline applied to our bulk RNA-seq data. Epithelial cell populations were first identified following the tutorial workflow of the Seurat R package (Satija et al. 2015), without applying a cell filtering step. Within the epithelial population, cancer cells were distinguished based on the presence of large-scale copy number variations (CNVs) inferred using the inferCNVpy Python package (https://infercnvpy.readthedocs.io/en/latest/index.html). CNV profiles were calculated using fibroblast and endothelial cell populations as reference non-malignant cells. For the head

and neck squamous cell carcinoma dataset, where raw data were not available, we utilized a publicly provided summary table containing TPM values and annotated cell types.

Viability assay of organoids

Organoid viability was assessed using the Celltiter-Glo 3D Assay kit (Promega, Cat No.G9681), following the manufacturer's instructions (see **Supplemental Methods**). Viability was calculated as the percentage of luminescence in doxycycline-treated samples related to the average luminescence of control groups.

Immunostaining and imaging of organoids

Whole-mount staining of human gastric organoids was performed as previously described (van Ineveld et al. 2020). Briefly, organoids were fixed with 4% paraformaldehyde (PFA) after depolymerizing the 3D matrix using ice-cold Cell Recovery solution (Corning). After washing with 0.1% PBS-Tween-20 and blocking with organoid washing buffer (0.1 % Triton X-100, 0.02 % SDS, 0.2 % bovine serum albumin (BSA) in 1× PBS), immunolabeling was performed with mouse anti-HA tag antibody (Santa Cruz, Cat No.sc-7392; 1:50) and rabbit anti-phospho-histone H2A.X antibody (CST, Cat No.2577S; 1:400) to detect HA-tagged APOBEC proteins and DNA damage, respectively. Secondary antibodies included Goat anti-mouse Alexa Fluor 488 (Thermo Fisher Scientific, Cat No.A-11001; 1:500) and donkey anti-rabbit Alexa Fluor 647 (Thermo Fisher Scientific, Cat No.A32795; 1:500). Nuclei were counter-stained with DAPI (Sigma-aldrich., Cat No.D9542; 1:1000). After washing, FUnGI clearing solution was added to the organoids, which were then mounted between two coverslips with a 0.25 mm-deep iSpacer (SunJin Lab, Cat No.IS213). Imaging was performed at least one hour after slide preparation. Imaging was performed with a Leica Stellaris 8 Confocal Microscope. Alexa Fluor 488, Alexa Fluor 647, and DAPI signals were obtained using either 40× or 63× objectives, with a digital zoom factor of 1- to 7-fold were used. The X/Y resolution was set to 1024 × 1024 pixels. Images were processed and analyzed using Adobe Photoshop.

Standard whole genome sequencing alignment

According to the manufacturer's protocol, DNA from clonal organoids was extracted using DNeasy Blood & Tissue Kit (QIAGEN, Cat No.69506) and libraries were constructed with TruSeq DNA PCR-Free Library Prep Kits (Illumina, Cat No.20015963). Whole-genome sequencing was performed on the NovaSeq 6000 with a mean 30× depth of coverage. Adapter sequences in the FASTAQ files were removed by cutadapt software (Martin 2011). For WGS and BotSeqS, reads were aligned to the human reference genome GRCh37 using BWA-MEM v0.7.17 (Li and Durbin 2010). Further processing, including sorting, marking duplication, and indel realignment, was conducted with SAMtools v1.9 (Li et al. 2009), Picard v2.1.0 (McKenna et al. 2010), and GATK tools v3.8.0 (McKenna et al. 2010). For *in vitro* deamination results, Bismark v0.23.0 (https://felixkrueger.github.io/Bismark/) were utilized for the mapping process.

BotSeqS library construction

Constructed libraries with TruSeq DNA PCR-Free Library Prep Kits (Illumina) were utilized for the BotSeqS libraries construction. The construction of BotSeqS libraries was based on the previous literature with slight modifications (Hoang et al. 2016). Briefly, after the quantification of DNA libraries with Quantification Kit ILLUMINA® Platforms (Roche, Cat No.KK48247), libraries equivalent to 4 pg of DNA were amplified with primers having a Y-adaptor sequence with a phosphorothioate bond(*) at the 3' end from IDT (Coralville, IA):

Forward: 5'-AATGATACGGCGACCACCGAG*A-3'

Reverse: 5'-CAAGCAGAAGACGGCATACGA*G-3'

PCR was performed using 20 cycles, following the protocol of the KAPA Library Amplification Kits (Roche). Libraries were sequenced as paired-end sequencing (2×151 bps) on the NovaSeq 6000.

534 **Calling copy number variations**

535 Copy number variations (CNVs) were accessed by Sequenza (Favero et al. 2015). CNVs in
536 segments smaller than 1 Mbp were considered false positives. After removing these short-
537 segment CNVs, final CNV profiles were obtained through a second run of the Sequenza.

538 **Confirming non-neoplasticity in primary human gastric organoid**

539 Germline variant calling was performed using the germline mutation calling mode in GATK
540 v4.0.12.0 (McKenna et al. 2010). The primary call set was first filtered using in-house scripts
541 based on the pysam module in Python (Li et al. 2009). Given the relevance of cancer driver
542 genes, the functional impact of variants was evaluated. The absence of CNV in the normal
543 gastric organoids was also confirmed (**Supplemental Fig. S15**).

544 **Detection of somatic mutations**

545 To detect single nucleotide variants and indels in clonal organoids, GATK Mutect2 v4.1.9
546 (McKenna et al. 2010) and Strelka2 v2.9.2 (Kim et al. 2018) were utilized. Bulk whole-
547 genome sequencing of 1st single-cell cloned lines, hGO$_{iA3A}$, TP53KO-hGO$_{iA3A}$, hGO$_{iA3B}$, and
548 TP53KO-hGO$_{iA3B}$ organoids, were utilized as matched normal for calling somatic mutations in
549 doxycycline-treated organoids. False-positive variants in each call set were filtered out with
550 in-house Python scripts annotating information within BAM files with the pysam module (see
551 **Supplemental Methods**). The filtered call sets from both Mutect2 and Strelka2 were
552 merged, and the union call set was utilized for downstream analysis. To exclude mutations
553 generated during the culture of 1st single-cell cloned lines, recurrent somatic mutations
554 observed across multiple samples were removed.

555 For BotSeqS, VarScan2 v2.3.9 (Koboldt et al. 2012) was used to increase the sensitivity.
556 Similarly, in-house Python scripts were utilized to remove false-positive calls (see
557 **Supplemental Methods**). Unlike with standard whole-genome sequencing, overexpressed
558 A3B induced the significantly increased C>T artifacts in the 5' head region during the

BotSeqS library construction process (**Supplemental Fig. S6A,B**). Thus, the false positive SNVs located within 100bp of 5' end or 3' end, considering reference strand, were removed. Additionally, rare variants from HEK293T cells, which were used to generate the conditioned medium, were observed. Thus, variants observed at least three times in the HEK293T BAM file were removed from the final call set.

Calculation of mutation rate in BotSeqS

Unlike standard WGS, the effective covered region was calculated for each BAM file. First, each read was evaluated using in-house scripts that considered DNA strand orientation and applied the following criteria to isolate effective DNA fragments: (1) median mapping quality > 20, (2) total depth of each type of reads ≥ 3. Only regions where both F1R2 and F2R1 reads were aligned were included in the covered region calculation. To account for the exclusion of mutations located within 100 bp of the extreme of read-ends during variant filtering (considering the reference genome strand), the total length of the covered region was adjusted by multiplying it by (151×2-110)/(151×2)). Mutation rates were calculated by dividing the number of observed mutations by this adjusted covered length. To normalize mutational burdens to the standard genome length, mutation rates were then multiplied by dividing the number of observed mutations by this adjusted covered length. To normalize mutational burdens to the standard genome length, mutation rates were then multiplied by the total genome length excluding repeat regions (3,041,373,115 bp) and further doubled.

Analysis of mutational signatures

Mutational signature analysis of single base substitutions (SBS) and small indels were carried out using non-negative least squares method. The mutational signature was represented by 96 patterns of SBS and 83 patterns of small indels (Alexandrov et al. 2020). Pre-learned catalogs of mutational signatures in the COSMIC (Sondka et al. 2024) were used to fit individual samples with a known set of signatures for each tissue type. SBS2 and SBS13 (known APOBEC associated signatures) were included for all cases.

585 **Calling RNA editings**

586 VarScan2 was utilized to identify RNA editing. WGS of 1st single-cell cloned lines served as
587 the paired normal reference. RNA editings were filtered with in-house Python script with the
588 pysam module (see **Supplemental Methods**). To compare the RNA editing counts across
589 samples, the number of RNA editings was normalized by a total base count. The total base
590 count was calculated using SAMtools, considering only reads with mapping and base quality
591 > 20. The lowest total base count (3.1Gb) was used as the normalization baseline. After
592 calculating the normalization factor, adjusted total depth of variant position and variant read
593 counts were filtered with the same criteria. Recurrent RNA editing sites were defined as
594 those observed in at least one sample treated with 0.1μg/ml or 3μg/ml doxycycline with the
595 normalized call set.

596 **Analysis of RNA editing signatures**

597 RNA editing signatures were obtained by a modified version of the mutational signature
598 extraction method described in previous studies (Youk et al. 2024; Alexandrov et al. 2013).
599 Briefly, non-negative matrix factorization (NMF) was utilized to disentangle an individual
600 RNA editing spectrum based on a notion of mixed spectra (see **Supplemental Methods**;
601 Cichocki et al. 2006; Roux et al.). Total 18 samples (each 3 samples of 0 μg/ml, 0.1 μg/ml,
602 and 3 μg/ml APOBEC3 exposure with hGO_{iA3A} and hGO_{iA3B}) were analyzed by splitting into
603 two subsets: A3A and A3B sets.

604 **Analysis of secondary structure of RNA editing sites**

605 The secondary structures of RNA editing sites were predicted as described previously (Jalili
606 et al. 2020). Briefly, a 41-bp sequence centered on each RNA editing site in the canonical
607 mRNA was used to assess secondary structure potential. Stem strength was calculated as
608 3×G/C pair + 1×A/T pair in stem. Among candidate structures, the most probable one was

selected based on the following hierarchical criteria: (1) highest stem strength, (2) greatest number of G/C pairs in the stem, and (3) smallest loop size.

Calling structural variations

Structural variations were identified using DELLY v0.7.6 (Rausch et al. 2012). Raw calls were filtered using in-house scripts from our previous reports (Lee et al. 2019). The final call set was manually reviewed by the Integrative Genomics Viewer (Robinson et al. 2011).

DNA deaminase activity assay

The cytosine deaminase activity assay against DNA was conducted based on the previous literature with slight modifications (Buisson et al. 2019; Sanchez and Buisson 2025). Briefly, a total volume of 50µl was prepared, containing either 8 µl of normalized cell lysates or recombinant APOBEC3A (1:8 dilution) from NEBNext® Enzymatic Methyl-seq Kit (New England Biolabs, E7120S), and 42 µl of reaction buffer. The reaction buffer consists of 20 pmol DNA oligonucleotide, 50mM Tris (pH 7.5), 1.5 units of uracil DNA glycosylase (New England Biolabs, M2080S), RNase A (0.1 µg/ml; Thermofisher Scientific, EN0531), and 10 mM EDTA. The DNA oligonucleotide was synthesized by Integrated DNA Technologies (IDT; Coralville, IA) with the sequence: 5'-(6-FAM)GCAAGCTGTTCAGCTTGCTGA-3'.

The reaction mixture was incubated at 37°C for 40 minutes, followed by the addition of 0.5 µl of 10N NaOH and further incubation at 95°C for 40 minutes. Then, 50µl of formamide was added, and the mixture was incubated 95°C for 10 minutes, followed by cooling at 4°C for 5 minutes. For analysis, 5 µl of each sample was mixed with an equal volume of Gel Loading Buffer II (AM8546G) and incubated at 95°C for 5 minutes. Separation of the DNA oligonucleotides was performed on a Novex™ TBE-Urea Gels, 15% (Invitrogen, EC6885BOX) by electrophoresis at 150 V for 60 minutes. Imaging was performed using the ibright™ CL750 Imaging System (Invitrogen).

***In vitro* deamination of DNA with recombinant APOBEC3B**

The NEBNext Enzymatic Methyl-seq (EM-seq) Kit (NEB, Cat No.E7120S) and the manufacturer's protocol were utilized for DNA library construction with slight modifications. 10 pg of input DNA were utilized for the library construction. For the deamination steps, recombinant APOBEC3B, synthesized by EUROPROTEIN INC. (North Brunswick Township, NJ), was used. The deamination step with APOBEC enzymes were conducted for 30 and 60 seconds. Library amplification steps followed the BotSeqS library construction.

Detection of deamination during *in vitro* denomination with APOBEC3B

The BotSeqS variant calling pipeline was utilized with slight modifications. Among the criteria, the distances from read ends were excluded. Initially, all filtered mutations were collected. Among mutations in grouped DNA, only those located in DNA fragments where only one strand was mapped were counted. To calculate the genome-wide mutation rates, the BotSeqS pipeline was utilized with the exception that cytosines or guanines were counted in a strand-specific manner. Since original methylated CpG sites were preserved during the library construction, both total base counts and mutation counts in CpG contexts were excluded from the analysis. To calculate mutation rates in DNA fragments containing at least one C>T variant, the genomic ranges of such fragments were identified using BEDTools (Quinlan and Hall 2010), considering the strand orientation. After this step, cytosines or guanines outside of CpG contexts were counted.

Analysis of 4bp context mutations

SNVs from 10 hGO_{iA3A} samples (excluding control samples) and 6 TP53KO-hGO_{iA3B} samples were utilized in the analysis. Among 567 PCAWG samples across eight cancer types with a high prevalence of APOBEC mutational activity - breast adenocarcinoma (BRCA; n=195), esophageal adenocarcinoma (ESAD; n=97), stomach adenocarcinoma (STAD; n=68), head and neck squamous cell carcinoma (HNSC; n=56), lung squamous cell carcinoma (LUSC; n=47), uterine corpus endometrial carcinoma (UCEC; n=44), lung adenocarcinoma (LUAD; n=37), bladder urothelial Carcinoma (BLCA; n=23) - only samples with a combined clonal

APOBEC-associated mutational burden (SBS2 + SBS13) greater than 5,000 were selected for this analysis (n=63). This subject included: LUSC (n=15), BRCA (n=12), BLCA (n=11), HNSC (n=13), LUAD (n=6), UCEC (n=3), ESAD (n=2), and STAD (n=1). Only clonal mutations were utilized for the analysis.

Calling clustered mutation

SigProfilerClusters (Bergstrom et al. 2022a), a Python module, was utilized to identify clustered mutations. FlexMix, R package (Leisch 2004), was utilized to classify the identified clustered mutations into *omikli* and *kataegis*. Since the tool determines the intermutation distance threshold through simulations that randomly distribute SNVs, the total number of SNVs influence the detection rate of clustered mutation events. To correct for the number of clustered mutation events, simulations were conducted (see **Supplemental Methods; Supplemental Figure S17**). The “drm” function in the drc, R package (Ritz et al. 2019) were utilized for the analysis. To compare clustered mutation events, 146 samples from the PCAWG database were selected based on the following criteria: (1) nine cancer types showing high prevalence of APOBEC mutational signatures; (2) samples with fewer than 500 SBS2+SBS13 were excluded in both our samples and PCAWG cancer samples to avoid bias.

Analysis of mutation rates depending on epigenetic marker

Relative risk of mutation rates between signal and non-signal regions were analyzed for each epigenetic marker, based on the previous studies (Nam et al. 2023; Supek and Lehner 2017). Genome-wide signals for each marker, including replication timing, were downloaded from Roadmap Epigenomics Consortium for eight cell types (E017,E114, E117, E118, E119, E122, E125, and E127). Fold-enrichment signals were averaged, and regions with values <1 were defined as bin0 (non-signal); all others were classified as signal-detected. SNVs were counted in each region, and relative risks were calculated, accounting for 3bp genomic context.

For APOBEC-associated mutations, cytosines in the TCN context were considered as background, and C>T and C>G substitutions at these sites were counted. For SBS5 and SBS40, all thymine bases except within TCN context were used as the reference, and T>A, T>G, T>C, C>T, and C>G substitutions were counted. C>A mutations were excluded to avoid overlapping signals with SBS1 and SBS18.

For replication timing and H3K27me3, signal-detected regions were further divided into four equal-length bins to assess fold-enrichment. For transcriptional activity, TPM values in each base were derived from RNA-seq of doxycycline-treated organoids (3 μg/ml, 48h). Using "hg19_refGene.txt" file from ANNOVAR (Wang et al. 2010), only genic regions were analyzed. Genes with TPM=0 were defined as bin0; TPM>0 regions were binned by quartiles (bin1=0.05, bin2=1.73, and bin3 & bin4=9.68). To account for interactions among transcription, H3K27me3, and replication timing, enrichment analysis was performed using the glm.nb() function from the MASS R package (Venables and Ripley 2003) as described in previous research (Supek and Lehner 2017).

Analysis of mutation rates depending on genomic location

SNVs located in previously described mappable regions were utilized throughout the analysis. Gene annotations from the "hg19_refGene.txt" file were utilized to match the additional information of position of SNVs. Classification of sub-genic regions (5'/3'UTR, protein coding sequence (CDS), and intron) and transcription strand orientation was also based on this gene information. All merged genic regions were used as reference for discrimination of genic and intergenic regions.

For sub-genic mutation rate comparisons, only non-overlapping genic regions and CDS regions flanked by introns were used, following a previously reported approach (Frigola et al. 2017).

Comparison of single nucleotide variants (SNVs) between reference genome versions

SNVs were additionally identified using human GRCh38 genome sequence. Coordinates of SNVs based on GRCh37 were converted to GRCh38 using BCFtools/liftover for comparative analysis (**Supplemental Fig. S16**; Genovese et al. 2024).

Publicly available datasets

Publicly available whole-genome sequencing data were utilized to demonstrate copy number variation in the normal human gastric organoid. WGS of blood from HC05 sample was utilized as the unpaired normal sample (EGA; accession number EGAS00001006213; Nam et al. 2023). To compare the 4bp-context preference and frequency of clustered mutation, SNV calls from the ICGC/TCGA Pan-Cancer Analysis of Whole-Genome (PCAWG) Consortium were utilized for the analysis. The call set data is available for download at https://docs.icgc-argo.org/docs/data-access/icgc-25k-data#relocated-icgc-25k-data.

We analyzed publicly available Smart-seq-based single-cell RNA-seq datasets from five cancer types: (1) lung adenocarcinoma (NCBI; accession number PRJNA591860; Maynard et al. 2020) (2) head and neck squamous cell carcinoma (NCBI; accession number PRJNA401654; GEO: GSE103322; Puram et al. 2017) (3) triple negative breast cancer (NCBI; PRJNA485423; GEO: GSE118390; Karaayvaz et al. 2018) (4) esophageal adenocarcinoma and esophageal squamous cell carcinoma (NCBI; PRJNA401501; Wu et al. 2018).

In addition, we analyzed publicly available whole transcriptomic sequencing data of SARS-CoV-2 infected human gastric organoid (NCBI; PRJNA643724; GEO: GSE153698; Giobbe et al. 2021) for the correlation between viral infections and expression of APOBEC family genes in human gastric organoid.

Quantification and statistical analysis

All statistical analyses were performed with R version 4.1.3 (R Core Team, Vienna, Austria). A two-tailed one-sample *t*-test was used to evaluate p-values for comparing APOBEC-associated SNVs and expression levels between the groups. Linear regressions were conducted using the basic 'lm' function in R to analyze the association among APOBEC-associated SNVs, ID9, SBS5, and SBS40. A chi-square test was utilized to evaluate p-values for comparing replication strand bias and transcription strand bias. A 95% confidence interval was used to determine the statistical range of continuous data.

DATA ACCESS

All raw and processed sequencing data generated in this study have been submitted to the Korean Nucleotide Archive (KoNA; https://kbds.re.kr/KRA) under accession number KAP240815. Essential in-house scripts used in this study are available on Zenodo (https://doi.org/10.5281/zenodo.12771074) and Supplemental Code.

COMPETING INTEREST STATEMENT

Y.S.J. is a genomic co-founder of Inocras Inc..

ACKNOWLEDGEMENTS

The authors thank Youngwon Cho (Epithelial Biology Center, Vanderbilt University Medical Center) for helping with the cell viability test, Myungsuk Choi (KAIST) for technical help for organoids, and Mia Petljak (New York University) for her valuable advice and feedback on the manuscript. This work was supported by the Young Investigator Grants from the Human Frontier Science Program (RGY0071/2018 to Y.S.J., B.-K.K., and H.S.); the National Research Foundation of Korea (Leading Researcher Program NRF-2020R1A3B2078973 to Y.S.J.); the Korea Bio Data Station (N24NM016-24 to J.L and J.W.P); and the Institute for Basic Science (IBS-R021-D1 to B.-K.K).

Y.S.J., B.-K.K., and H.S. designed the experiments. J.-H.K. provided human gastric epithelium sample from biopsy. Y.J.B. established organoids from primary human gastric tissues. J.L. and J.W.P. helped basic bioinformatic works (alignment and calling somatic variants). J-H.L. and J.Y. conducted vector cloning. Y.A. and T.K. conducted the transformation of organoids, with J-H.L. and J.Y. providing advice. Y.A. performed organoid culture, clonal expansion, and DNA/RNA extraction. B.-K.K. and H.K. provided training in organoids culture technologies. Y.A. performed cell viability analysis. J-H.L. performed immunohistochemistry. S.A.O. conducted *in vitro* deamination experiments and most of the library construction including WGS and RNA-seq. Y.A., J.-H.P., and K.Y. conducted library construction for duplex sequencing analysis. Y.A. conducted most bioinformatic analyses, including alignment, mutation calling, duplex sequencing analysis, and analysis of expression levels with bulk RNA-seq data, with S.P., J.Y., and Y.S.J. providing advice. Y.A. and Jo.L. conducted quantitative and statistical data analysis. Y.A. and Jo.L. conducted mutational signature analysis including RNA editing. W.H.L. helped with the construction of pipeline for analysis of duplex sequencing. Y.A. and C.H.N. conducted epigenomic analysis of variants and comparing variants based on two reference genomes GRCh37 and GRCh38. H.L., J.H, and T.M.K. conducted western blotting experiment.

REFERENCES

Abascal F, Harvey LMR, Mitchell E, Lawson ARJ, Lensing SV, Ellis P, Russell AJC, Alcantara RE, Baez-Ortega A, Wang Y, et al. 2021. Somatic mutation landscapes at single-molecule resolution. *Nature* **593**: 405–410.

Alexandrov LB, Kim J, Haradhvala NJ, Huang MN, Tian Ng AW, Wu Y, Boot A, Covington KR, Gordenin DA, Bergstrom EN, et al. 2020. The repertoire of mutational signatures in human cancer. *Nature* **578**: 94–101.

Alexandrov LB, Nik-Zainal S, Wedge DC, Campbell PJ, Stratton MR. 2013. Deciphering signatures of mutational processes operative in human cancer. *Cell Rep* **3**: 246–259.

Alonso de la Vega A, Temiz NA, Tasakis R, Somogyi K, Salgueiro L, Zimmer E, Ramos M, Diaz-Jimenez A, Chocarro S, Fernández-Vaquero M, et al. 2023. Acute expression of human APOBEC3B in mice results in RNA editing and lethality. *Genome Biol* **24**: 267.

Amador V, Ge S, Santamaría PG, Guardavaccaro D, Pagano M. 2007. APC/C(Cdc20) controls the ubiquitin-mediated degradation of p21 in prometaphase. *Mol Cell* **27**: 462–473.

Amouroux R, Campalans A, Epe B, Radicella JP. 2010. Oxidative stress triggers the preferential assembly of base excision repair complexes on open chromatin regions. *Nucleic Acids Res* **38**: 2878–2890.

Bartfeld S, Bayram T, van de Wetering M, Huch M, Begthel H, Kujala P, Vries R, Peters PJ, Clevers H. 2015. In vitro expansion of human gastric epithelial stem cells and their responses to bacterial infection. *Gastroenterology* **148**: 126–136.e6.

Bergstrom EN, Kundu M, Tbeileh N, Alexandrov LB. 2022. Examining clustered somatic mutations with SigProfilerClusters. *Bioinformatics* **38**: 3470–3473.

Bergstrom EN, Luebeck J, Petljak M, Khandekar A, Barnes M, Zhang T, Steele CD, Pillay N, Landi MT, Bafna V, et al. 2022b. Mapping clustered mutations in cancer reveals APOBEC3 mutagenesis of ecDNA. *Nature* **602**: 510–517.

Buisson R, Langenbucher A, Bowen D, Kwan EE, Benes CH, Zou L, Lawrence MS. 2019. Passenger hotspot mutations in cancer driven by APOBEC3A and mesoscale genomic features. *Science* **364**. http://dx.doi.org/10.1126/science.aaw2872.

Burns MB, Lackey L, Carpenter MA, Rathore A, Land AM, Leonard B, Refsland EW, Kotandeniya D, Tretyakova N, Nikas JB, et al. 2013. APOBEC3B is an enzymatic source of mutation in breast cancer. *Nature* **494**: 366–370.

Carpenter MA, Temiz NA, Ibrahim MA, Jarvis MC, Brown MR, Argyris PP, Brown WL, Starrett GJ, Yee D, Harris RS. 2023. Mutational impact of APOBEC3A and APOBEC3B in a human cell line and comparisons to breast cancer. *PLoS Genet* **19**: e1011043.

Cazzalini O, Scovassi AI, Savio M, Stivala LA, Prosperi E. 2010. Multiple roles of the cell cycle inhibitor p21(CDKN1A) in the DNA damage response. *Mutat Res* **704**: 12–20.

Chan K, Roberts SA, Klimczak LJ, Sterling JF, Saini N, Malc EP, Kim J, Kwiatkowski DJ, Fargo DC, Mieczkowski PA, et al. 2015. An APOBEC3A hypermutation signature is distinguishable from the signature of background mutagenesis by APOBEC3B in human cancers. *Nat Genet* **47**: 1067–1072.

816 Choi J-H, Pfeifer GP. 2005. The role of DNA polymerase eta in UV mutational spectra. *DNA*
817 *Repair* **4**: 211–220.

818 Cichocki A, Zdunek R, Amari S. 2006. New algorithms for non-negative matrix factorization
819 in applications to blind source separation. In *2006 IEEE International Conference on*
820 *Acoustics Speed and Signal Processing Proceedings*, IEEE
821 http://ieeexplore.ieee.org/document/1661352/.

822 Dananberg A, Striepen J, Rozowsky JS, Petljak M. 2024. APOBEC Mutagenesis in Cancer
823 Development and Susceptibility. *Cancers* **16**.
824 http://dx.doi.org/10.3390/cancers16020374.

825 Delbos F, De Smet A, Faili A, Aoufouchi S, Weill J-C, Reynaud C-A. 2005. Contribution of
826 DNA polymerase eta to immunoglobulin gene hypermutation in the mouse. *J Exp Med*
827 **201**: 1191–1196.

828 DeWeerd RA, Németh E, Póti Á, Petryk N, Chen C-L, Hyrien O, Szüts D, Green AM. 2022.
829 Prospectively defined patterns of APOBEC3A mutagenesis are prevalent in human
830 cancers. *Cell Rep* **38**: 110555.

831 Dobin A, Davis CA, Schlesinger F, Drenkow J, Zaleski C, Jha S, Batut P, Chaisson M,
832 Gingeras TR. 2013. STAR: ultrafast universal RNA-seq aligner. *Bioinformatics* **29**: 15–
833 21.

834 Durfee C, Temiz NA, Levin-Klein R, Argyris PP, Alsøe L, Carracedo S, Alonso de la Vega A,
835 Proehl J, Holzhauer AM, Seeman ZJ, et al. 2023. Human APOBEC3B promotes tumor
836 development in vivo including signature mutations and metastases. *Cell Rep Med* **4**:
837 101211.

838 Favero F, Joshi T, Marquard AM, Birkbak NJ, Krzystanek M, Li Q, Szallasi Z, Eklund AC.
839 2015. Sequenza: allele-specific copy number and mutation profiles from tumor
840 sequencing data. *Ann Oncol* **26**: 64–70.

841 Fixman B, Díaz-Gay M, Qiu C, Margaryan T, Lee B, Chen XS. 2024. Validation of the
842 APOBEC3A-Mediated RNA Single Base Substitution Signature and Proposal of Novel
843 APOBEC1, APOBEC3B, and APOBEC3G RNA Signatures. *J Mol Biol* **436**: 168854.

844 Frigola J, Sabarinathan R, Mularoni L, Muiños F, Gonzalez-Perez A, López-Bigas N. 2017.
845 Reduced mutation rate in exons due to differential mismatch repair. *Nat Genet* **49**:
846 1684–1692.

847 Fujii M, Matano M, Nanki K, Sato T. 2015. Efficient genetic engineering of human intestinal
848 organoids using electroporation. *Nat Protoc* **10**: 1474–1485.

849 Gaebler A-M, Hennig A, Buczolich K, Weitz J, Welsch T, Stange DE, Pape K. 2020.
850 Universal and Efficient Electroporation Protocol for Genetic Engineering of
851 Gastrointestinal Organoids. *J Vis Exp*. http://dx.doi.org/10.3791/60704.

852 Genovese G, Rockweiler NB, Gorman BR, Bigdeli TB, Pato MT, Pato CN, Ichihara K,
853 McCarroll SA. 2024. BCFtools/liftover: an accurate and comprehensive tool to convert
854 genetic variants across genome assemblies. *Bioinformatics* **40**: btae038.

855 Giobbe GG, Bonfante F, Jones BC, Gagliano O, Luni C, Zambaiti E, Perin S, Laterza C,
856 Busslinger G, Stuart H, et al. 2021. SARS-CoV-2 infection and replication in human
857 gastric organoids. *Nat Commun* **12**: 6610.

Gnatt AL, Cramer P, Fu J, Bushnell DA, Kornberg RD. 2001. Structural basis of transcription: an RNA polymerase II elongation complex at 3.3 A resolution. *Science* **292**: 1876–1882.

Green AM, Landry S, Budagyan K, Avgousti DC, Shalhout S, Bhagwat AS, Weitzman MD. 2016. APOBEC3A damages the cellular genome during DNA replication. *Cell Cycle* **15**: 998–1008.

Hoang ML, Kinde I, Tomasetti C, McMahon KW, Rosenquist TA, Grollman AP, Kinzler KW, Vogelstein B, Papadopoulos N. 2016. Genome-wide quantification of rare somatic mutations in normal human tissues using massively parallel sequencing. *Proc Natl Acad Sci U S A* **113**: 9846–9851.

Hoopes JI, Cortez LM, Mertz TM, Malc EP, Mieczkowski PA, Roberts SA. 2016. APOBEC3A and APOBEC3B Preferentially Deaminate the Lagging Strand Template during DNA Replication. *Cell Rep* **14**: 1273–1282.

Jager M, Blokzijl F, Kuijk E, Bertl J, Vougioukalaki M, Janssen R, Besselink N, Boymans S, de Ligt J, Pedersen JS, et al. 2019. Deficiency of nucleotide excision repair is associated with mutational signature observed in cancer. *Genome Res* **29**: 1067–1077.

Jalili P, Bowen D, Langenbucher A, Park S, Aguirre K, Corcoran RB, Fleischman AG, Lawrence MS, Zou L, Buisson R. 2020. Quantification of ongoing APOBEC3A activity in tumor cells by monitoring RNA editing at hotspots. *Nat Commun* **11**: 2971.

Karaayvaz M, Cristea S, Gillespie SM, Patel AP, Mylvaganam R, Luo CC, Specht MC, Bernstein BE, Michor F, Ellisen LW. 2018. Unravelling subclonal heterogeneity and aggressive disease states in TNBC through single-cell RNA-seq. *Nat Commun* **9**: 3588.

Kazanov MD, Roberts SA, Polak P, Stamatoyannopoulos J, Klimczak LJ, Gordenin DA, Sunyaev SR. 2015. APOBEC-Induced Cancer Mutations Are Uniquely Enriched in Early-Replicating, Gene-Dense, and Active Chromatin Regions. *Cell Rep* **13**: 1103–1109.

Kim J, Mouw KW, Polak P, Braunstein LZ, Kamburov A, Kwiatkowski DJ, Rosenberg JE, Van Allen EM, D'Andrea A, Getz G. 2016. Somatic ERCC2 mutations are associated with a distinct genomic signature in urothelial tumors. *Nat Genet* **48**: 600–606.

Kim K, Shi AB, Kelley K, Chen XS. 2023. Unraveling the Enzyme-Substrate Properties for APOBEC3A-Mediated RNA Editing. *J Mol Biol* **435**: 168198.

Kim S, Scheffler K, Halpern AL, Bekritsky MA, Noh E, Källberg M, Chen X, Kim Y, Beyter D, Krusche P, et al. 2018. Strelka2: fast and accurate calling of germline and somatic variants. *Nat Methods* **15**: 591–594.

Koboldt DC, Zhang Q, Larson DE, Shen D, McLellan MD, Lin L, Miller CA, Mardis ER, Ding L, Wilson RK. 2012. VarScan 2: somatic mutation and copy number alteration discovery in cancer by exome sequencing. *Genome Res* **22**: 568–576.

Law EK, Levin-Klein R, Jarvis MC, Kim H, Argyris PP, Carpenter MA, Starrett GJ, Temiz NA, Larson LK, Durfee C, et al. 2020. APOBEC3A catalyzes mutation and drives carcinogenesis in vivo. *J Exp Med* **217**. http://dx.doi.org/10.1084/jem.20200261.

Lawrence MS, Stojanov P, Polak P, Kryukov GV, Cibulskis K, Sivachenko A, Carter SL, Stewart C, Mermel CH, Roberts SA, et al. 2013. Mutational heterogeneity in cancer and the search for new cancer-associated genes. *Nature* **499**: 214–218.

Lawson ARJ, Abascal F, Coorens THH, Hooks Y, O'Neill L, Latimer C, Raine K, Sanders MA, Warren AY, Mahbubani KTA, et al. 2020. Extensive heterogeneity in somatic mutation and selection in the human bladder. *Science* **370**: 75–82.

Lee J-H, Kim S, Han S, Min J, Caldwell B, Bamford A-D, Rocha ASB, Park J, Lee S, Wu S-HS, et al. 2022. p57 imposes the reserve stem cell state of gastric chief cells. *Cell Stem Cell* **29**: 826–839.e9.

Lee JJ-K, Park S, Park H, Kim S, Lee J, Lee J, Youk J, Yi K, An Y, Park IK, et al. 2019. Tracing Oncogene Rearrangements in the Mutational History of Lung Adenocarcinoma. *Cell* **177**: 1842–1857.e21.

Leisch F. 2004. FlexMix: A general framework for finite mixture models and latent class regression inR. *J Stat Softw* **11**. http://www.jstatsoft.org/v11/i08/.

Li B, Dewey CN. 2011. RSEM: accurate transcript quantification from RNA-Seq data with or without a reference genome. *BMC Bioinformatics* **12**: 323.

Li H, Durbin R. 2010. Fast and accurate long-read alignment with Burrows-Wheeler transform. *Bioinformatics* **26**: 589–595.

Li H, Handsaker B, Wysoker A, Fennell T, Ruan J, Homer N, Marth G, Abecasis G, Durbin R, 1000 Genome Project Data Processing Subgroup. 2009. The Sequence Alignment/Map format and SAMtools. *Bioinformatics* **25**: 2078–2079.

Love MI, Huber W, Anders S. 2014. Moderated estimation of fold change and dispersion for RNA-seq data with DESeq2. *Genome Biol* **15**: 550.

Maciejowski J, Chatzipli A, Dananberg A, Chu K, Toufektchan E, Klimczak LJ, Gordenin DA, Campbell PJ, de Lange T. 2020. APOBEC3-dependent kataegis and TREX1-driven chromothripsis during telomere crisis. *Nat Genet* **52**: 884–890.

Martínez-Ruiz C, Black JRM, Puttick C, Hill MS, Demeulemeester J, Larose Cadieux E, Thol K, Jones TP, Veeriah S, Naceur-Lombardelli C, et al. 2023. Genomic-transcriptomic evolution in lung cancer and metastasis. *Nature* **616**: 543–552.

Martin M. 2011. Cutadapt removes adapter sequences from high-throughput sequencing reads. *EMBnet.journal* **17**: 10–12.

Matsushima K, Yang D, Oppenheim JJ. 2022. Interleukin-8: An evolving chemokine. *Cytokine* **153**: 155828.

Maynard A, McCoach CE, Rotow JK, Harris L, Haderk F, Kerr DL, Yu EA, Schenk EL, Tan W, Zee A, et al. 2020. Therapy-Induced Evolution of Human Lung Cancer Revealed by Single-Cell RNA Sequencing. *Cell* **182**: 1232–1251.e22.

McKenna A, Hanna M, Banks E, Sivachenko A, Cibulskis K, Kernytsky A, Garimella K, Altshuler D, Gabriel S, Daly M, et al. 2010. The Genome Analysis Toolkit: a MapReduce framework for analyzing next-generation DNA sequencing data. *Genome Res* **20**: 1297–1303.

Mihara E, Hirai H, Yamamoto H, Tamura-Kawakami K, Matano M, Kikuchi A, Sato T, Takagi J. 2016. Active and water-soluble form of lipidated Wnt protein is maintained by a serum glycoprotein afamin/α-albumin. https://elifesciences.org/articles/11621 (Accessed August 30, 2024).

Nam CH, Youk J, Kim JY, Lim J, Park JW, Oh SA, Lee HJ, Park JW, Won H, Lee Y, et al.

2023. Widespread somatic L1 retrotransposition in normal colorectal epithelium. *Nature* **617**: 540–547.

Naumann JA, Argyris PP, Carpenter MA, Gupta HB, Chen Y, Temiz NA, Zhou Y, Durfee C, Proehl J, Koniar BL, et al. 2023. DNA Deamination Is Required for Human APOBEC3A-Driven Hepatocellular Carcinoma In Vivo. *Int J Mol Sci* **24**. http://dx.doi.org/10.3390/ijms24119305.

Nik-Zainal S, Alexandrov LB, Wedge DC, Van Loo P, Greenman CD, Raine K, Jones D, Hinton J, Marshall J, Stebbings LA, et al. 2012a. Mutational processes molding the genomes of 21 breast cancers. *Cell* **149**: 979–993.

Nik-Zainal S, Van Loo P, Wedge DC, Alexandrov LB, Greenman CD, Lau KW, Raine K, Jones D, Marshall J, Ramakrishna M, et al. 2012b. The life history of 21 breast cancers. *Cell* **149**: 994–1007.

Nordentoft I, Lamy P, Birkenkamp-Demtröder K, Shumansky K, Vang S, Hornshøj H, Juul M, Villesen P, Hedegaard J, Roth A, et al. 2014. Mutational context and diverse clonal development in early and late bladder cancer. *Cell Rep* **7**: 1649–1663.

Okazaki R, Okazaki T, Sakabe K, Sugimoto K, Sugino A. 1968. Mechanism of DNA chain growth. I. Possible discontinuity and unusual secondary structure of newly synthesized chains. *Proc Natl Acad Sci U S A* **59**: 598–605.

Otlu B, Díaz-Gay M, Vermes I, Bergstrom EN, Zhivagui M, Barnes M, Alexandrov LB. 2023. Topography of mutational signatures in human cancer. *Cell Rep* **42**: 112930.

Park S, Mali NM, Kim R, Choi J-W, Lee J, Lim J, Park JM, Park JW, Kim D, Kim T, et al. 2021. Clonal dynamics in early human embryogenesis inferred from somatic mutation. *Nature* **597**: 393–397.

Petljak M, Alexandrov LB, Brammeld JS, Price S, Wedge DC, Grossmann S, Dawson KJ, Ju YS, Iorio F, Tubio JMC, et al. 2019. Characterizing Mutational Signatures in Human Cancer Cell Lines Reveals Episodic APOBEC Mutagenesis. *Cell* **176**: 1282–1294.e20.

Petljak M, Dananberg A, Chu K, Bergstrom EN, Striepen J, von Morgen P, Chen Y, Shah H, Sale JE, Alexandrov LB, et al. 2022. Mechanisms of APOBEC3 mutagenesis in human cancer cells. *Nature* **607**: 799–807.

Pleguezuelos-Manzano C, Puschhof J, Rosendahl Huber A, van Hoeck A, Wood HM, Nomburg J, Gurjao C, Manders F, Dalmasso G, Stege PB, et al. 2020. Mutational signature in colorectal cancer caused by genotoxic pks E. coli. *Nature* **580**: 269–273.

Puram SV, Tirosh I, Parikh AS, Patel AP, Yizhak K, Gillespie S, Rodman C, Luo CL, Mroz EA, Emerick KS, et al. 2017. Single-Cell Transcriptomic Analysis of Primary and Metastatic Tumor Ecosystems in Head and Neck Cancer. *Cell* **171**: 1611–1624.e24.

Quinlan AR, Hall IM. 2010. BEDTools: a flexible suite of utilities for comparing genomic features. *Bioinformatics* **26**: 841–842.

Rausch T, Zichner T, Schlattl A, Stütz AM, Benes V, Korbel JO. 2012. DELLY: structural variant discovery by integrated paired-end and split-read analysis. *Bioinformatics* **28**: i333–i339.

Rhind N, Gilbert DM. 2013. DNA replication timing. *Cold Spring Harb Perspect Biol* **5**: a010132.

Ritz C, Jensen SM, Gerhard D, Streibig JC. 2019. *Dose-Response Analysis Using R*. CRC Press.

Roberts SA, Lawrence MS, Klimczak LJ, Grimm SA, Fargo D, Stojanov P, Kiezun A, Kryukov GV, Carter SL, Saksena G, et al. 2013. An APOBEC cytidine deaminase mutagenesis pattern is widespread in human cancers. *Nat Genet* **45**: 970–976.

Robinson JT, Thorvaldsdóttir H, Winckler W, Guttman M, Lander ES, Getz G, Mesirov JP. 2011. Integrative genomics viewer. *Nat Biotechnol* **29**: 24–26.

Roux L, J., Weninger, F.J. and Hershey, J.R., 2015. Sparse NMF–half-baked or well done?. Mitsubishi Electric Research Labs (MERL), Cambridge, MA, USA, Tech. Rep., no. TR2015-023, 11:13-15. https://www.merl.com/publications/docs/TR2015-023.

Saini N, Roberts SA, Sterling JF, Malc EP, Mieczkowski PA, Gordenin DA. 2017. APOBEC3B cytidine deaminase targets the non-transcribed strand of tRNA genes in yeast. *DNA Repair (Amst)* **53**: 4–14.

Sanchez A, Buisson R. 2025. An in vitro cytidine deaminase assay to monitor APOBEC activity on DNA. *Methods Enzymol* **713**: 201–219.

Sanchez A, Ortega P, Sakhtemani R, Manjunath L, Oh S, Bournique E, Becker A, Kim K, Durfee C, Temiz NA, et al. 2024. Mesoscale DNA features impact APOBEC3A and APOBEC3B deaminase activity and shape tumor mutational landscapes. *Nat Commun* **15**: 2370.

Satija R, Farrell JA, Gennert D, Schier AF, Regev A. 2015. Spatial reconstruction of single-cell gene expression data. *Nat Biotechnol* **33**: 495–502.

Sondka Z, Dhir NB, Carvalho-Silva D, Jupe S, Madhumita, McLaren K, Starkey M, Ward S, Wilding J, Ahmed M, et al. 2024. COSMIC: a curated database of somatic variants and clinical data for cancer. *Nucleic Acids Res* **52**: D1210–D1217.

Supek F, Lehner B. 2017. Clustered Mutation Signatures Reveal that Error-Prone DNA Repair Targets Mutations to Active Genes. *Cell* **170**: 534–547.e23.

The ICGC/TCGA Pan-Cancer Analysis of Whole Genomes Consortium. 2020. Pan-cancer analysis of whole genomes. *Nature* **578**: 82–93. https://doi.org/10.1038/s41586-020-1969-6.

van Ineveld RL, Ariese HCR, Wehrens EJ, Dekkers JF, Rios AC. 2020. Single-Cell Resolution Three-Dimensional Imaging of Intact Organoids. *J Vis Exp*. http://dx.doi.org/10.3791/60709.

Venables WN, Ripley BD. 2003. *Modern Applied Statistics with S*. Springer Science & Business Media.

Vieira VC, Soares MA. 2013. The role of cytidine deaminases on innate immune responses against human viral infections. *Biomed Res Int* **2013**: 683095.

Wang K, Li M, Hakonarson H. 2010. ANNOVAR: functional annotation of genetic variants from high-throughput sequencing data. *Nucleic Acids Res* **38**: e164.

Wang Y, Robinson PS, Coorens THH, Moore L, Lee-Six H, Noorani A, Sanders MA, Jung H, Katainen R, Heuschkel R, et al. 2023. APOBEC mutagenesis is a common process in normal human small intestine. *Nat Genet* **55**: 246–254.

1026 Wilson MH, Coates CJ, George AL Jr. 2007. PiggyBac transposon-mediated gene transfer in
1027 human cells. *Mol Ther* **15**: 139–145.

1028 Woodard LE, Wilson MH. 2015. piggyBac-ing models and new therapeutic strategies.
1029 *Trends Biotechnol* **33**: 525–533.

1030 Wu H, Yu J, Li Y, Hou Q, Zhou R, Zhang N, Jing Z, Jiang M, Li Z, Hua Y, et al. 2018. Single-
1031 cell RNA sequencing reveals diverse intratumoral heterogeneities and gene signatures
1032 of two types of esophageal cancers. *Cancer Lett* **438**: 133–143.

1033 Wu T, Lyu R, You Q, He C. 2020. Kethoxal-assisted single-stranded DNA sequencing
1034 captures global transcription dynamics and enhancer activity in situ. *Nat Methods* **17**:
1035 515–523.

1036 Wu Y-Y, Tsai H-F, Lin W-C, Hsu P-I, Shun C-T, Wu M-S, Hsu P-N. 2007. Upregulation of
1037 CCL20 and recruitment of CCR6+ gastric infiltrating lymphocytes in Helicobacter pylori
1038 gastritis. *Infect Immun* **75**: 4357–4363.

1039 Yoshida K, Gowers KHC, Lee-Six H, Chandrasekharan DP, Coorens T, Maughan EF, Beal
1040 K, Menzies A, Millar FR, Anderson E, et al. 2020. Tobacco smoking and somatic
1041 mutations in human bronchial epithelium. *Nature* **578**: 266–272.

1042 Youk J, Kwon HW, Kim R, Ju YS. 2021. Dissecting single-cell genomes through the clonal
1043 organoid technique. *Exp Mol Med* **53**: 1503–1511.

1044 Youk J, Kwon HW, Lim J, Kim E, Kim T, Kim R, Park S, Yi K, Nam CH, Jeon S, et al. 2024.
1045 Quantitative and qualitative mutational impact of ionizing radiation on normal cells. *Cell*
1046 *Genom* **4**: 100499.

FIGURE LEGENDS

Figure 1. Overview of conditional APOBEC (APOBEC3A or APOBEC3B) overexpression models with human gastric organoids.

(A) Experimental design of the study. Schematic illustration of genetic engineering, cloning, and sequencing (whole-genome sequencing, duplex sequencing, and bulk RNA-seq) is shown. Dox, doxycycline.

(B) Changes of morphology and mCherry fluorescence during 48 hours with 0.1 μg/ml doxycycline treatment. (top) hGO_{iA3A} lines and (bottom) hGO_{iA3B} lines. Scale bars represent 1mm.

(C) Inducible expression of APOBEC3A (A3A) or APOBEC3B (A3B) enzymes in hGO_{iA3A} and hGO_{iA3B} lines, respectively, following 3 μg/ml doxycycline treatment for 48 hours.

(D) Expression levels of APOBEC3A (A3A) or APOBEC3B (A3B) in each line following 0.1 μg/ml and 3 μg/ml doxycycline treatment for 48 hours. (left) hGO_{iA3A} lines (n=3 per condition) and (right) hGO_{iA3B} lines (n=3 per condition). Data are presented as mean ± 95% confidence interval. Statistical significance was determined using a *t*-test: *p < 0.05, **p < 0.005, ***p < 0.0005, ****p < 0.00005.

(E) Changes of viability of each line following 0.1 μg/ml and 3 μg/ml doxycycline treatment for 48 hours (n=4 per each condition). Data are presented as mean ± 95% confidence interval.

(F) Differentially expressed genes upon APOBEC (A3A or A3B) overexpression following 0.1 μg/ml doxycycline treatment for 48 hours. (top) hGO_{iA3A} line and (bottom) hGO_{iA3B} line. adj.pval, adjusted p-value.

(G) Subcellular localization of overexpressed A3A and A3B following 3 μg/ml doxycycline treatment for 48 hours in each line. (left) hGO_{iA3A} line and (right) hGO_{iA3B} line. Scale bars represent 50 μm.

(H) γ-H2AX foci following 3 μg/ml doxycycline treatment for 48 hours in each line. (left) hGO_{iA3A} line and (right) hGO_{iA3B} line. Scale bars represent 50μm.

Figure 2. Mutational impact of APOBEC-associated single base substitutions in DNA and RNA.

(A) Mutational burden of SNVs following APOBEC overexpression (A3A or A3B), measured by whole-genome sequencing of the clones and duplex DNA sequencing. The number of SNVs measured by the duplex DNA sequencing was normalized per diploid genome. (left) hGO_{iA3A} lines and (right) hGO_{iA3B} lines.

(B) Mutational burden of APOBEC-associated SNVs in the hGO_{iA3A} and TP53KO-hGO_{iA3A} clone sequencing**.** The number of A3A-associated SNVs (SBS2+SBS13) in hGO_{iA3A} and TP53KO-hGO_{iA3A} clones under each condition. Statistical significance was determined using a *t*-test: *p < 0.05, **p < 0.005, ***p < 0.0005, and ****p < 0.00005.

(C) Number of A3A-associated SNVs (SBS2+SBS13; normalized per diploid genome) in BotSeqS results for hGO_{iA3A} lines under each doxycycline treatment condition. Black lines represent 95% confidence intervals based on a *Poisson* distribution.

(D) Mutational burden of APOBEC-associated SNVs in the hGO_{iA3B} and TP53KO-hGO_{iA3B} clone sequencing**.** The number of A3B-associated SNVs (SBS2+SBS13) in hGO_{iA3B} and TP53KO-hGO_{iA3B} clones under each condition. Statistical significance was determined using a *t*-test: *p < 0.05, **p < 0.005, ***p < 0.0005, and ****p < 0.00005.

(E) Number of A3B-associated SNVs (SBS2+SBS13; normalized per diploid genome) in BotSeqS results for hGO_{iA3B} lines under each doxycycline treatment condition. Black lines represent 95% confidence intervals based on a *Poisson* distribution.

(F) Mutational burden and spectra of APOBEC-associated SNVs in each experimental condition. The number of SNVs in BotSeqS results were normalized per diploid genome. (left) hGO_{iA3A} lines and (right) hGO_{iA3B} lines.

(G) Number of C>U RNA editing in bulk RNA-seq in hGO_{iA3A} lines (n=3 per condition), normalized per 3.1 Gb of mapped bases.

(H) Spectra of RNA editing in trinucleotide contexts in hGO_{iA3A} lines.

(I) Number of C>U RNA editing in bulk RNA-seq in hGO_{iA3A} lines (n=3 per condition), normalized per 3.1 Gb of mapped bases.

(J) Spectra of RNA editing in trinucleotide contexts in hGO_{iA3B} lines.

Figure 3. Deamination activity of APOBEC3B *in vitro.*

(A) Cytosine deaminase activities of cell lysates from hGO_{iA3A} and hGO_{iA3B} lines following 3 µg/ml doxycycline treatment for 48 hours. NC, negative control; rA3A, recombinant A3A

(B) Sequences in randomly selected 100 read pairs in recombinant APOBEC3B exposed cell-free denatured genomic single stranded DNA for 60 seconds.

(C) Deamination rate of unmethylated cytosines in recombinant A3B-exposed cell-free DNA fragments. CTRL, negative control, 30s, DNA exposed for 30 seconds, 60s, DNA exposed for 60 seconds.

Figure 4. Characteristics of A3A-associated mutational signatures.

(A) Context preference of A3A between YpTpCpA and RpTpCpA context in hGO_{iA3A} lines and APOBEC-associated mutations in hypermutant cancer samples. Only PCAWG cancer samples with a combined APOBEC-associated clonal mutational burden (SBS2 + SBS13) greater than 5,000 were selected (n=63) among eight cancer types with a high prevalence of APOBEC mutational activity. lung adenocarcinoma (n=15), breast adenocarcinoma (n=12), bladder urothelial carcinoma (n=11), head and neck squamous cell carcinoma (n=13), lung adenocarcinoma (n=6), uterine corpus endometrial carcinoma (n=3), esophageal adenocarcinoma (n=2), and stomach adenocarcinoma (n=1). Dashed black line, expected; orange line, hGO_{iA3A}; dark brown line, cancer.

(B) Correlation between A3A-associated base substitutions and ID9 contributing indels among hGO_{iA3A} lines.

(C) Associations between A3A-associated (SBS2 and SBS13) and age-associated (SBS5 and SBS40) SNVs among hGO_{iA3A} lines and TP53KO-hGO_{iA3A} clones.

(D) Changes in *POLH* gene expression (translesion synthesis DNA polymerase) following *A3A* induction in hGO_{iA3A} and TP53KO-hGO_{iA3A} lines.

Figure 5. Landscape of APOBEC3A-associated clustered mutation.

(A) Observed-to-expected ratios of the intermutational distances between SNVs in each clone. Data are presented as mean ± standard error.

(B) Frequencies of clustered mutation events (*omikli* and *kataegis*) among A3A-associated base substitutions in clones and cancer genomes.

(C) Proportions of classic (in TpCpN context) and non-classical mutations (in non-TpCpN and NpTpN) in SBS2, SBS13, and *kataegis* regions in the clones.

(D) Comparison of expected and observed number of SNVs in the non-TpCpN context within *kataegis* regions.

(E) Schematic representation of strand-switching *kataegis*.

(F) Strand-switching frequencies of *omikli* and *kataegis* across classes of clustered mutation events.

(G) A complex strand-switching *kataegis* involving five switches found in clone A3A_1st_C3_3µg-5.

(H) Enrichments of minor strand mutations in the TpCpN context in strand-switching *kataegis* events.

Figure 6. Genomic and epigenomic distribution of APOBEC3A-associated mutations.

(A) Correlations between epigenetic markers and A3A-associated substitutions.

(B) Fold change of mutation rates of A3A-associated SNVs across genomic regions grouped by replication timing. Data are presented as mean ± 95% confidence interval.

(C) Mutation rates on the leading and lagging DNA strands during replication. Statistical significance was determined using chi-square test: ****p<0.00005.

(D) Fold change of mutation rates of A3A-associated SNVs across genomic regions grouped by transcription. Data are presented as mean ± 95% confidence interval.

(E) Mutation rates on the transcribed and untranscribed DNA strands during transcription. Statistical significance was determined using a chi-square test: ***p<0.0005.

(F) Mutation rates across sub-genic regions (5'UTR, introns, protein coding sequences

(CDS), and 3'UTR) in hGO_{iA3A} clones (left) and TP53KO-hGO_{iA3A} clones (right). Red dashed line, average genome-wide mutation rate.

Figure 1

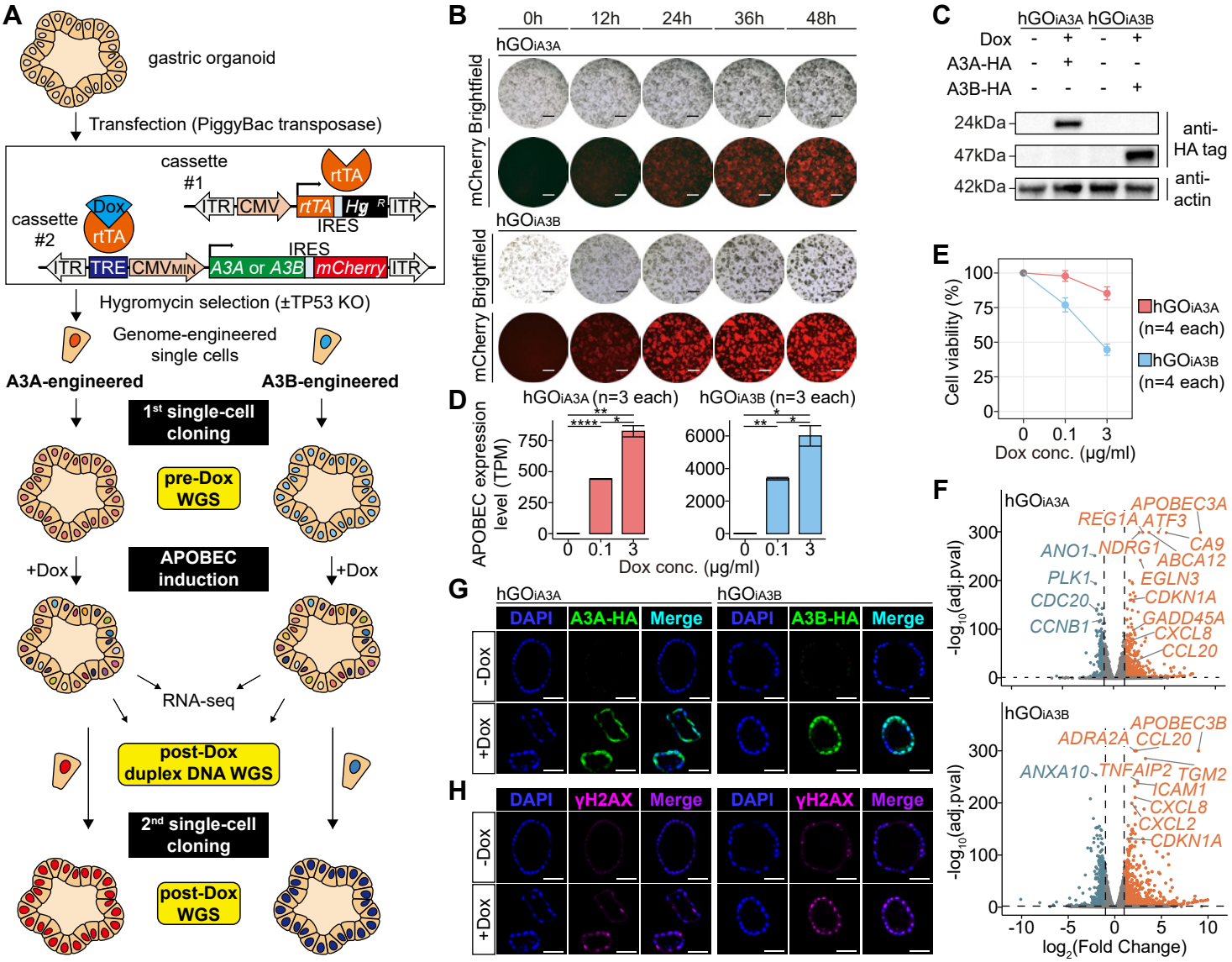

Figure 2

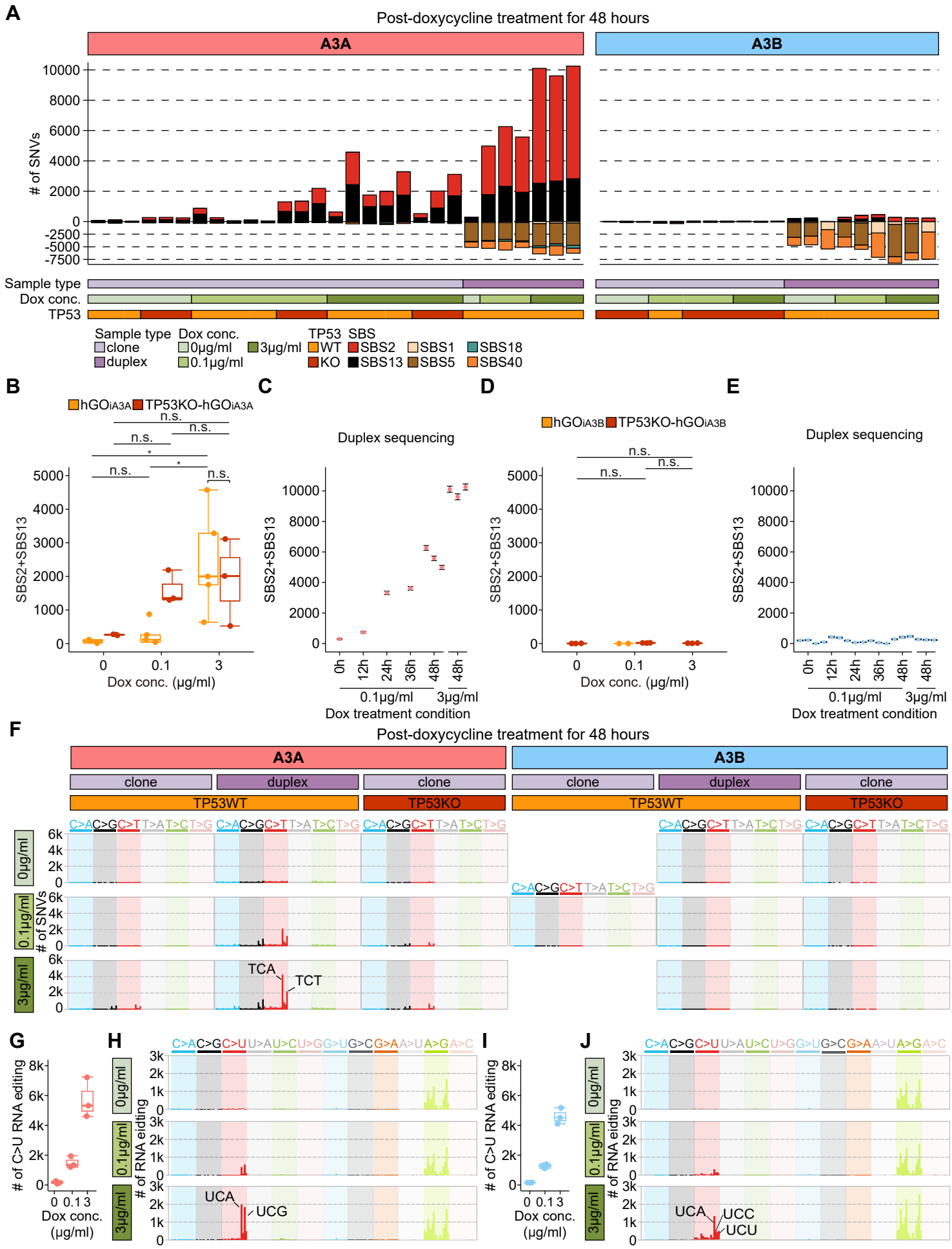

Figure 3

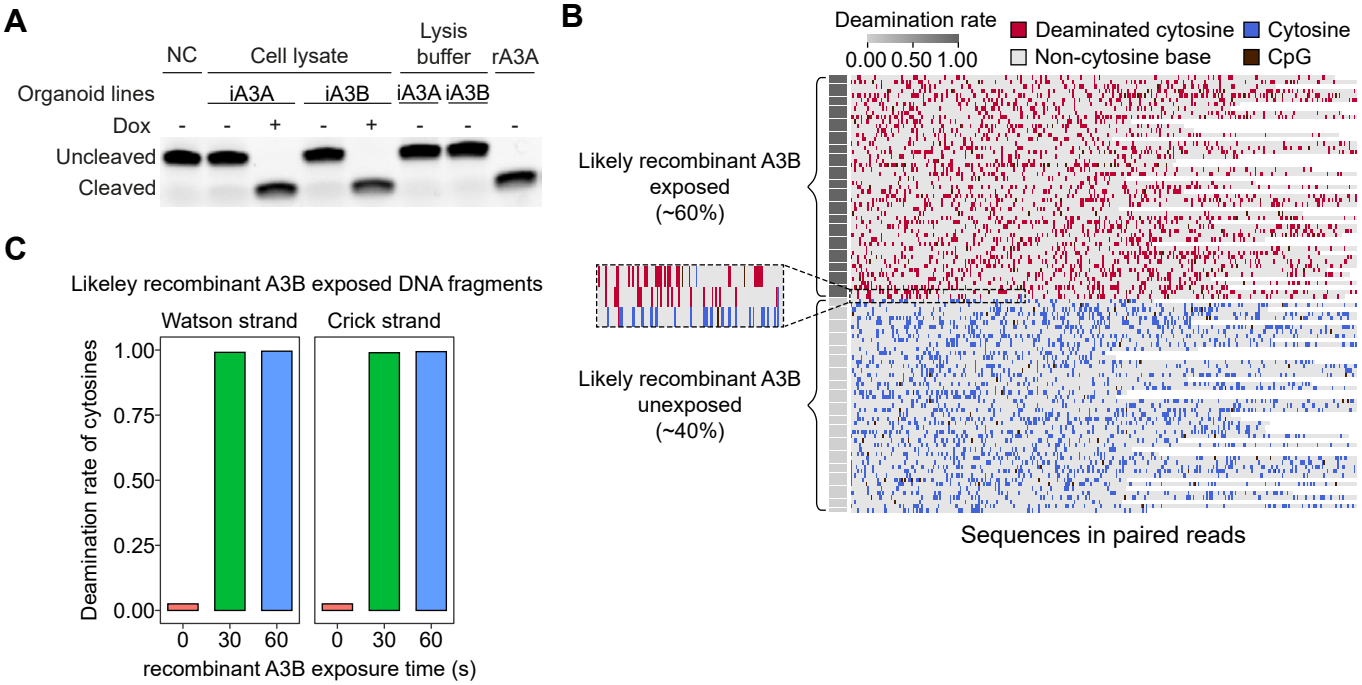

Figure 4

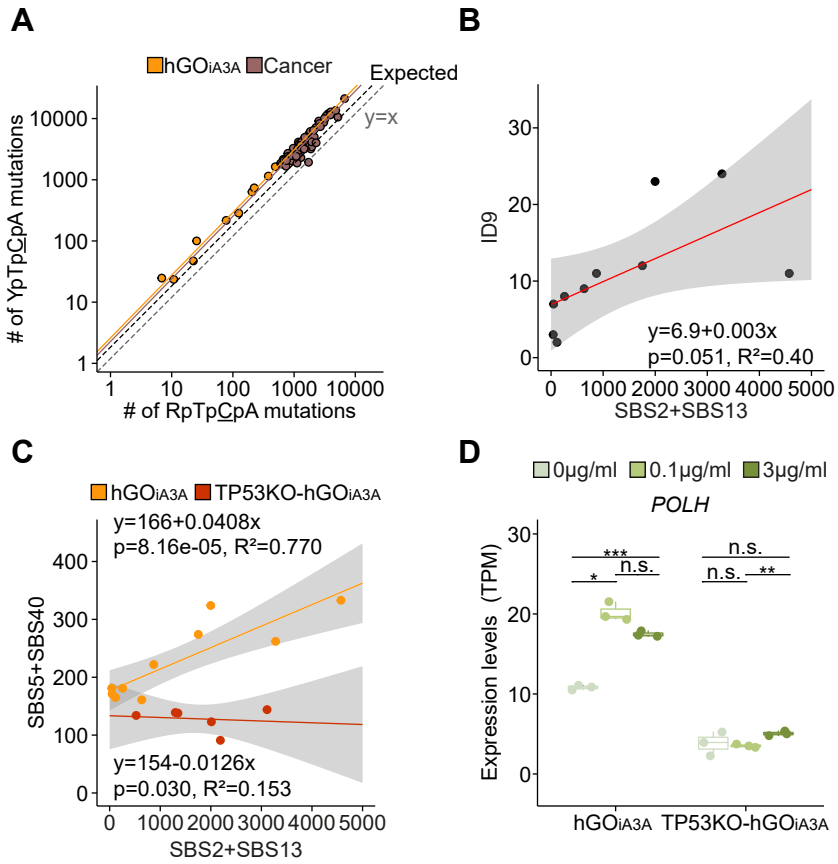

Figure 5

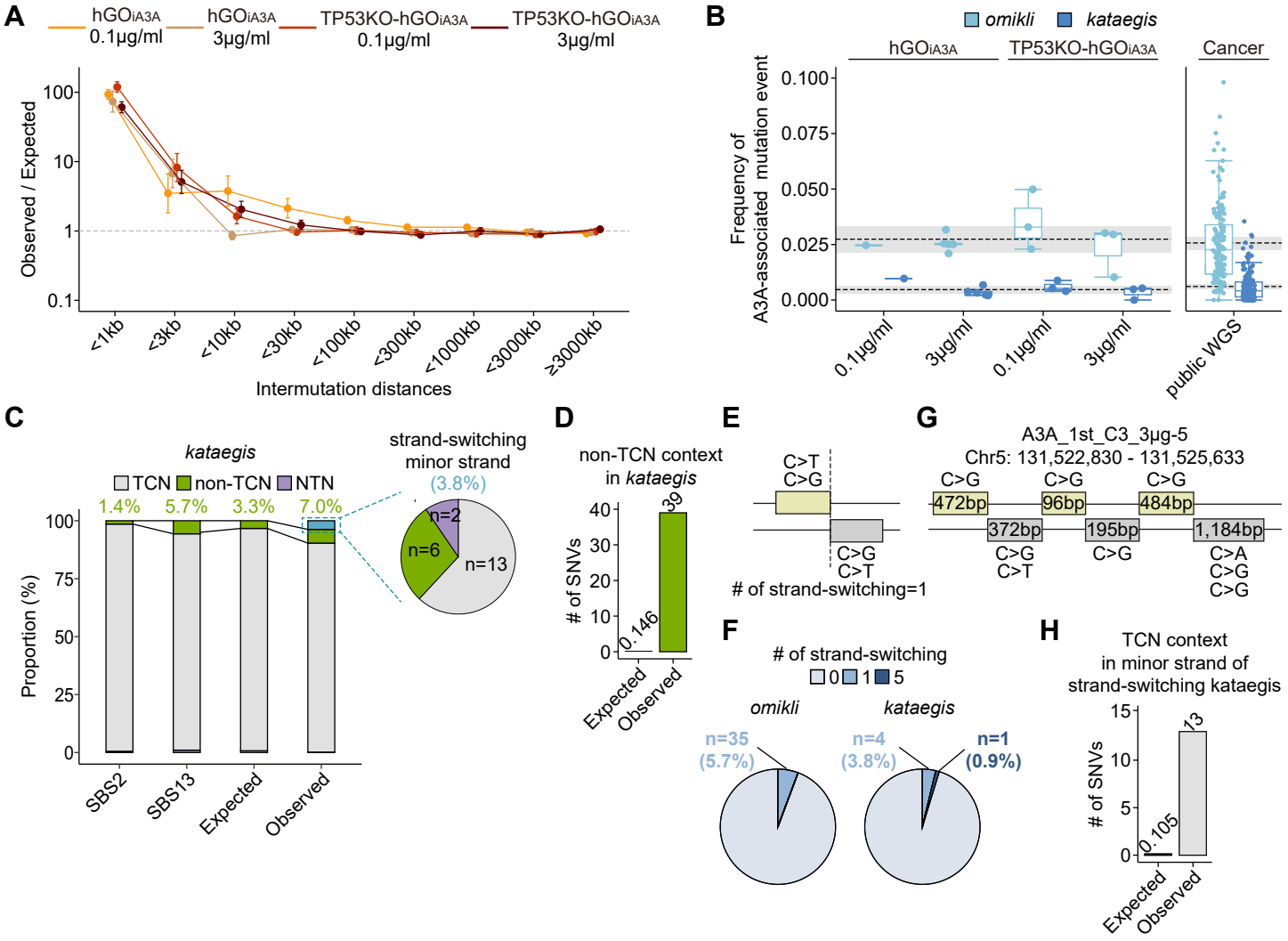

Figure 6

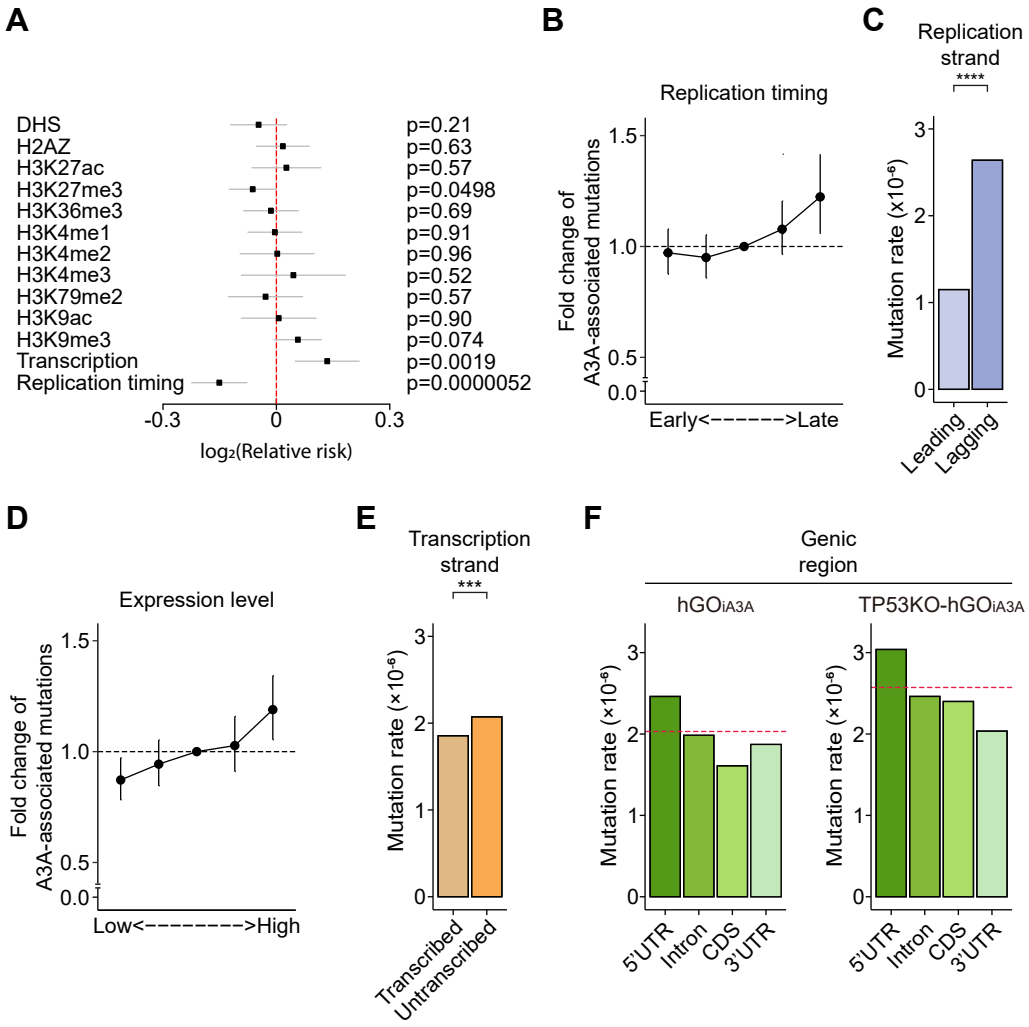

APOBEC3A drives deaminase mutagenesis in human gastric epithelium

Yohan An, Ji-Hyun Lee, Joonoh Lim, et al.

Genome Res. published online August 26, 2025
Access the most recent version at doi:10.1101/gr.280338.124